J. Fluid Mech. (2010), *vol.* 663, *pp.* 401–433.
doi:10.1017/S0022112010003563

The effects of mass transfer on the global stability of the rotating-disk boundary layer

CHRISTIAN THOMAS[1] AND CHRISTOPHER DAVIES[2]†

[1]School of Mathematics and Statistics, University of Western Australia, Perth, WA 6009, Australia
[2]School of Mathematics, Cardiff University, Cardiff CF24 4AG, UK

(Received 30 July 2009; revised 29 June 2010; accepted 1 July 2010;
first published online 12 October 2010)

Numerical simulations were conducted to investigate the effects of surface suction and injection on the global behaviour of linear disturbances in the rotating-disk boundary layer. This extends earlier work, which considered the case with no mass transfer. For disturbances in the genuine base flow, where radially inhomogeneity is retained, mass injection at the disk surface led to behaviour that remained qualitatively similar to that which was found when there was no mass transfer. The initial development of disturbances within the absolutely unstable region involved temporal growth and upstream propagation, as should be anticipated for an absolute instability. However, this did not persist indefinitely. Just as for the case without mass transfer, the simulation results suggested that convective behaviour would eventually dominate, for all the Reynolds numbers investigated. In marked contrast, the results obtained for flows with mass suction indicate a destabilization due to the effects of the base-flow radial inhomogeneity. It was possible to identify disturbances excited within the absolutely unstable region that grew continually, with a temporal growth rate that increased as the disturbance evolved. The strong locally stabilizing effect of suction on the absolute instability, which gives rise to large increases in critical Reynolds numbers, appears to be obtainable only at the expense of introducing a new form of global instability. Analogous forms of global behaviour can be found in impulse solutions of the linearized complex Ginzburg–Landau equation. These solutions were deployed to interpret and make comparisons with the numerical simulation results. They illustrate how the long-term behaviour of a disturbance can be determined by the precise balance between radial increases in temporal growth rates, corresponding shifts in temporal frequencies and diffusion/dispersion effects. This balance provides some insight into why disturbances that are absolutely unstable, for the homogenized version of the rotating-disk boundary-layer flow, may become, in the genuine radially inhomogeneous flow, either globally stable or globally unstable, depending on the level of mass transfer that is applied at the disk surface.

Key words: absolute/convective instability, boundary layer stability, transition to turbulence

1. Introduction

Mass transfer can be used to control the stability of fluid boundary layers and their transition from a laminar to a turbulent state. It is usually the case that uniform

† Email address for correspondence: DaviesC9@cardiff.ac.uk

suction through a bounding wall surface has the effect of stabilizing a laminar boundary layer, while the opposite effect from injection is destabilizing and promotes the transition to turbulence. An example of the potential benefits of suction is given in the study made by Hall, Malik & Poll (1984), which showed that suction has a stabilizing effect on the attachment-line boundary layer associated with the leading edge of a swept wing. Injection can also have some technological advantages, despite its generally destabilizing influence. For instance, it was shown by Sparrow & Gregg (1960) to be useful in cooling turbine blades and the surfaces of high-speed aircraft.

It was first noted by Batchelor (1951) that the system of ordinary differential equations governing the steady flow in the rotating-disk boundary layer, as derived using von Kármán (1921) similarity variables, could be readily extended to include mass transfer at the disk surface. Stuart (1954) then obtained the corresponding solutions for the velocity profiles. Gregory & Walker (1960) conducted a physical experiment to study the effects of uniform suction on the rotating-disk boundary layer. They found that the Reynolds numbers for the onset of crossflow instability and transition to turbulence could be raised greatly as the level of the suction was increased.

The crossflow instability is inviscid in nature, being associated with an inflection point in profiles of the mean velocity. It was originally discovered by Gray (1952) in his experimental study of the flow over a swept wing. Gregory, Stuart & Walker (1955) conducted a theoretical and experimental investigation for the rotating-disk flow and found physical evidence for the presence of the crossflow instability, in the form of stationary vortices which gave a readily visualized imprint in the shear stress patterns on the disk surface. In the rotating-disk context, crossflow instability is frequently designated as Type 1 mode of instability. Apart from this mode of instability, there exist at least two other modes. The Type 2 mode is essentially viscous and is destabilized by the Coriolis forces present within the rotating-disk boundary layer. It was first discovered by Faller & Kaylor (1966) within the Ekman layer; Malik (1986) gave evidence for its presence within the von Kármán flow. A third mode (Type 3) was discovered by Mack (1985). Because this mode propagates radially inwards and is spatially damped, it was not considered to be of any physical significance until its role in promoting absolute instability was uncovered.

1.1. *Absolute instability*

Absolutely unstable behaviour was identified by Lingwood (1995), using the Briggs (1964) method, which classifies the singularities in the dispersion relationship,

$$D(\alpha, \omega; Re, \beta) = 0, \tag{1.1}$$

that arise when waves propagating in opposite directions coalesce to yield pinch points. Here α, β are the radial and azimuthal wavenumbers, ω is the temporal frequency and Re denotes the Reynolds number. Absolute instability was shown to result from the coalescence of the Type 1 and 3 modes, with a critical Reynolds number given as $Re = 507.3$ (Lingwood 1995, 1997). An inviscid form of the absolute instability was also identified, using a complementary analysis for the high-Reynolds-number limit.

The critical Reynolds number that was computed for the absolute instability is very close to experimentally determined values for the onset of transition to turbulence. Taking the average onset value from a selection of previous transition experiments to be $Re = 513 \pm 3$ %, Lingwood was thus able to suggest that the absolute instability that she had discovered could provide the primary mechanism for transition to turbulence in the rotating-disk boundary layer. She provided further evidence to establish this

claim using the results obtained from her own physical experiment (Lingwood 1996). However, despite her experimental re-confirmation of the coincidence between the onset of transition and the appearance of absolute instability, Lingwood was not able to discover any strong selection of a temporal frequency that could be associated with this. The appearance of a dominant frequency would have been anticipated if the absolute instability had given rise to a temporally growing global mode of disturbance, and hence to a pattern of behaviour akin, for example, to that which leads to the presentation of a distinct shedding frequency in absolutely unstable wake flows.

Pier (2003) conducted a secondary stability analysis for the rotating-disk flow, perturbed by the finite-amplitude crossflow vortices that he expected to develop because of the absolute instability. He showed that this perturbed flow was itself absolutely unstable, thus providing a possible explanation for the absence in physical experiments of any dominant temporal frequency due to the primary absolute instability. The secondary absolute instability could be expected to quickly overwhelm the primary absolute instability upon which it grew, giving rise to a complex multi-frequency transitional flow, but still leading to the kind of sharp onset of transition that had been observed in experiments.

Lingwood (1997) extended her theoretical studies to include the effects of uniform mass transfer through the rotating disk surface. Using the usual non-dimensional parameter $\boldsymbol{a}$ to specify the degree of mass transfer, it was found that for $\boldsymbol{a} = -1$ ($\boldsymbol{a} < 0$ corresponds to uniform injection) the critical Reynolds number for absolute instability is approximately 202, less than half that observed for the case with zero mass transfer. Whereas for $\boldsymbol{a} = 1$ ($\boldsymbol{a} > 0$ corresponds to uniform suction) the critical Reynolds number is approximately 1861, almost four times that observed for the case with zero mass transfer. For the case $\boldsymbol{a} = 0.4$, absolute instability was found to arise for $Re \approx 803$. This is in apparent conflict with the results that were obtained in the earlier physical experiment conducted by Gregory & Walker (1960), where transition to turbulence was observed to occur for $Re \approx 632$ when $\boldsymbol{a} = 0.4$. Nevertheless, Lingwood proposed that absolute instability might still have been responsible for the onset of transition in the experimental study, if the imperfections of the physical apparatus had reduced the effectiveness of suction in stabilizing the flow.

It should be noted that the dispersion relation analysis that underlies the identification of an absolute instability necessitates the use of an actual or assumed spatial homogeneity for the basic flow. In the case of the rotating-disk boundary layer, this requirement can only be met by enforcing an artificial form of homogenization along the radial direction, because for the genuine base flow, the magnitudes of both the radial and azimuthal components scale linearly with the radius. Davies, Thomas & Carpenter (2007) discussed the impact of this radial inhomogeneity of the base flow and highlighted its consequences for the interpretation of the temporal frequency ω and the azimuthal wavenumber β, when both of these are non-dimensionalized in the usual locally based fashion. For instance, careful attention must be paid to draw out the physical significance of the single complex value of the temporal frequency that was identified by Lingwood (1995) for the absolute instability in the inviscid limit. The complex value that she computed actually represents temporal frequencies and temporal growth rates that vary linearly with the radius, when a suitable interpretation of the behaviour in the inviscid limit is made for disturbances evolving in the genuine inhomogeneous rotating-disk boundary layer. More generally, for the viscous case at finite Reynolds numbers, an assessment of the balance between the appropriately measured radial variations in frequencies and growth rates is helpful for understanding why the presence of an absolute instability may not be sufficient

to give rise to any globally unstable forms of disturbance behaviour. (This will be discussed and illustrated in more detail later.)

1.2. *Numerical simulations*

Davies & Carpenter (2003) conducted numerical simulations to study the evolution of linearized disturbances in the genuine, radially inhomogeneous, rotating-disk flow. The linearity of the governing equations, together with the lack of any azimuthal variation in the basic flow, meant that the disturbances were separable with respect to the azimuthal coordinate θ. Thus, simulations could be undertaken for modes with a prescribed azimuthal dependence $\sim \exp(\mathrm{i}n\theta)$, where n is the integer-valued azimuthal mode number. However, the radially varying nature of the basic flow precludes any separability with respect to the radial coordinate. Disturbances with a specified radial wavenumber can only be studied individually if the base flow is artificially homogenized.

The outcomes from the simulations carried out by Davies & Carpenter (2003) are schematically illustrated in figure 1, for the radially inhomogeneous flow with no mass transfer. Figure 1(a) displays the wavepacket evolution for a disturbance that is impulsively excited radially inboard from the absolutely unstable region, while figure 1(b) displays the corresponding evolution when the disturbance is triggered within the absolutely unstable region. In the latter configuration, the trailing edge of the disturbance wavepacket propagates radially inwards, at least initially, in a manner that is consistent with absolute instability and temporal growth. Nonetheless, such behaviour does not persist indefinitely; as the trailing edge of the disturbance nears the boundary of the region where absolute instability is anticipated, it is found to reverse direction and propagate radially outwards. Davies & Carpenter (2003) found that the absolute instability did not give rise to any sustained, temporally growing, oscillations that could be associated with an unstable linear global mode that had an amplitude dependence of the form

$$A \sim \exp(-\mathrm{i}\omega_g t), \tag{1.2}$$

where $\omega_g = \omega_{g,r} + \mathrm{i}\omega_{g,i}$ is the complex global frequency, and $\omega_{g,i} > 0$ for instability. Instead, convective behaviour was found to dominate the disturbance response, for all of the Reynolds numbers that were considered, even those well within the region of absolute instability.

A recent experimental investigation by Othman & Corke (2006) supports the results of the numerical simulation studied by Davies & Carpenter (2003). In their carefully conducted physical experiment, Othman & Corke were able to trace the development of disturbances with a much smaller amplitude than had been feasible in the experiments of Lingwood (1996). They considered disturbances that were impulsively excited radially inboard from the region of absolute instability, at a radial position that matched that which had been chosen by Lingwood. With their much reduced forcing amplitude, Othman & Corke (2006) could observe wavepackets that had a trailing edge that moved radially outwards with a positive velocity at all of the radial locations that it passed through, including those within the absolutely unstable region. The kind of behaviour that they documented was thus in good agreement with the numerical simulation results for linearized disturbances that are depicted in figure 1(a). In contrast, Lingwood had found that the trailing edge of her disturbance wavepacket seemed to asymptote towards a constant radial position at the boundary of the absolutely unstable region of the flow; the trailing edge moved more and more

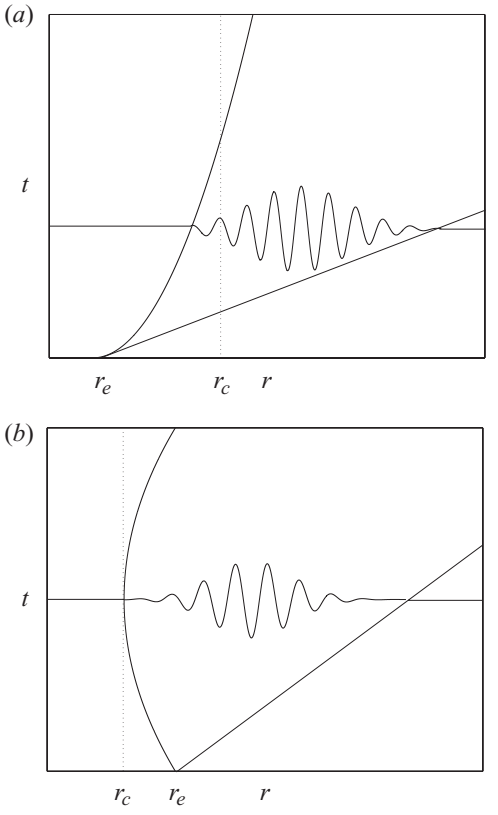

FIGURE 1. Sketch of the typical spatio-temporal evolution for a wavepacket excited in the rotating-disk boundary layer, as revealed by Davies & Carpenter (2003). It is seen later that the same kind of behaviour is found in the numerical simulation results for cases with normal injection applied at the disk surface. (*a*) Impulse excitation for $r_e < r_c$; (*b*) impulse excitation for $r_e > r_c$, where r_e is the radius at which the impulse is centred and r_c denotes the critical radius/Reynolds number for the onset of absolute instability.

slowly, appearing to become stationary as it reached the radius corresponding to the critical Reynolds number for the absolute instability.

It is the intention of the current study to extend the findings of Davies & Carpenter (2003) to rotating-disk boundary layers with mass transfer through the disk surface. Our initial concern will be with reporting the interconnections that hold between the absolute instability and the global behaviour, in so far as these can be discovered by means of linearized numerical simulations. However, perhaps more importantly, we shall also seek to provide some theoretical explanation of the simulation results, using the modelling approach that was first described by Davies *et al.* (2007) for the case with no mass transfer. By studying the parametric dependence that arises when the degree of mass transfer is systematically varied, we expose a broader range of possibilities, which affords more scope for making sense of the balance that persists between local and global behaviour. The remainder of this paper is set out as follows. The subsequent section describes the base-flow equations and the velocity–vorticity formulation that is used to determine the disturbance evolution, taking into account the effects of mass transfer. In § 3 the results from the radially inhomogeneous flow simulations are presented and discussed. In § 4 an understanding of the results is sought by making

comparisons with impulse solutions of the linearized complex Ginzburg–Landau equation. Some comments about possible forms of nonlinear disturbance behaviour are made in § 5. Finally, conclusions are given in § 6.

2. Mathematical formulation

2.1. *The basic flow*

The disk is taken to be infinite in diameter and rotates in an incompressible fluid with kinematic viscosity ν^* at a constant angular velocity Λ^* about the vertical axis that passes through the centre of the disk. Cylindrical polar coordinates are used, where r^* is taken to be the radial distance from the vertical axis of rotation, θ is the azimuthal angle and z^* is the normal direction. The domain above the disk is taken to be infinite, $z^* > 0$. (Here an asterisk denotes dimensional quantities.) In what follows, all quantities are defined in the frame of reference that rotates with the disk.

If $\boldsymbol{U}^* = \left(U_r^*, U_\theta^*, U_z^*\right)$ denotes the dimensional velocity, the von Kármán (1921) similarity solution is found by setting

$$\boldsymbol{U}^* = \left(r^*\Lambda^* F(z), r^*\Lambda^* G(z), \delta^*\Lambda^* H(z)\right), \tag{2.1}$$

where F, G, H represent non-dimensional profiles for the radial, azimuthal and normal base-flow velocity components, respectively. The wall-normal coordinate is $z = z^*/\delta^*$, where $\delta^* = (\nu^*/\Lambda^*)^{1/2}$ is the constant dimensional boundary-layer thickness that is used to non-dimensionalize lengths. Using the circumferential speed of the rotating disk at a reference radius r_a^* to non-dimensionalize the velocities, the base flow can be written in the form

$$\boldsymbol{U}_B = \left(\frac{r}{Re}F(z), \frac{r}{Re}G(z), \frac{1}{Re}H(z)\right), \tag{2.2}$$

with the Reynolds number defined as

$$Re = \frac{(r_a^*\Lambda^*)\delta^*}{\nu^*} = \frac{r_a^*}{\delta^*} = r_a. \tag{2.3}$$

It may be seen that the non-dimensionalization is such that the radial coordinate corresponding to any chosen radial position is equal to the Reynolds number defined using that position as the reference point to specify the scaling of the velocities. For the purpose of making comparisons with the results of stability investigations conducted using a radially homogenized approximation, the radial dependence of the basic flow can be artificially removed by simply setting $r = r_a$ in (2.2).

On substituting the assumed form of the similarity solution (2.1) into the Navier–Stokes equations for the fluid in the rotating frame of reference, the following system of non-dimensional equations is obtained for the basic flow:

$$F^2 + F'H - (G+1)^2 = F'', \tag{2.4}$$

$$2F(G+1) + G'H = G'', \tag{2.5}$$

$$2F + H' = 0, \tag{2.6}$$

where the prime denotes differentiation with respect to the normal direction z. Equations (2.4)–(2.6) are solved subject to the boundary conditions

$$F(0) = G(0) = 0, \qquad H(0) = \frac{H_0^*}{\nu^*\Lambda^*} = -\boldsymbol{a}, \tag{2.7}$$

$$F(z \to \infty) = 0, \qquad G(z \to \infty) = -1, \tag{2.8}$$

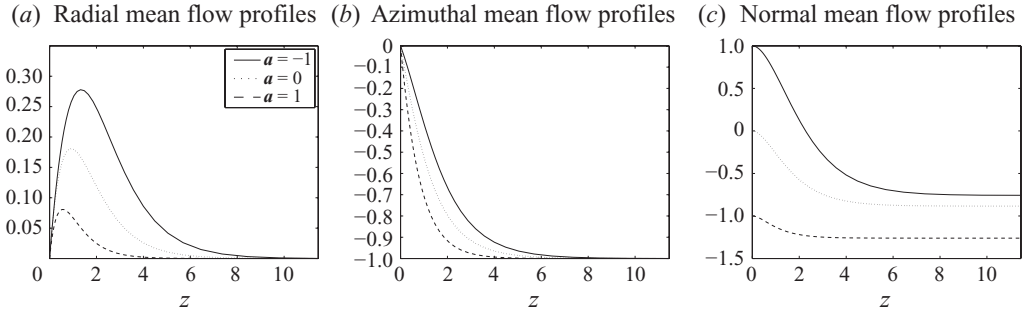

FIGURE 2. The base-flow velocity profiles for the radial (F), azimuthal (G) and normal (H) components for the von Kármán flow over a rotating disk with $\boldsymbol{a} = 0$ (dotted lines), $\boldsymbol{a} = 1$ (solid lines) and $\boldsymbol{a} = -1$ (dashed lines).

where H_0^* is the constant dimensional velocity at the disk surface, so that $\boldsymbol{a}$ is a positive constant for suction through the disk and is negative for mass injection.

Numerical solutions of the set of equations (2.4)–(2.8) for the velocity profiles are plotted in figure 2, for $\boldsymbol{a} = -1, 0$ and 1. In all three cases, the radial velocity profile is inflectional. For the flow with injection, the magnitude of the radial velocity profile increases, so the three-dimensionality of the boundary layer is enhanced. However, the normal flow at infinity becomes less negative. The opposite is true for suction; the magnitude of the radial velocity profile decreases, while the downwards flow at infinity is more pronounced.

2.2. *Velocity–vorticity formulation for perturbations*

The total velocity and vorticity fields are decomposed as

$$\boldsymbol{U} = \boldsymbol{U}_B + \boldsymbol{u}, \qquad \boldsymbol{\Omega} = \boldsymbol{\Omega}_B + \boldsymbol{\omega}, \tag{2.9}$$

where $\boldsymbol{U}_B$ and $\boldsymbol{\Omega}_B = \nabla \times \boldsymbol{U}_B$ correspond to the undisturbed base flow, while the velocity and vorticity perturbation variables may be represented as

$$\boldsymbol{u} = (u_r, u_\theta, u_z), \qquad \boldsymbol{\omega} = (\omega_r, \omega_\theta, \omega_z). \tag{2.10}$$

Taking the primary vorticity and velocity variables to be the three perturbation components $\{\omega_r, \omega_\theta, u_z\}$, the linearized Navier–Stokes equations are fully equivalent to the following set of equations (Davies & Carpenter 2001):

$$\frac{\partial \omega_r}{\partial t} + \frac{1}{r}\frac{\partial N_z}{\partial \theta} - \frac{\partial N_\theta}{\partial z} - \frac{2}{Re}\left(\omega_\theta + \frac{\partial u_z}{\partial r}\right) = \frac{1}{Re}\left(\left(\nabla^2 - \frac{1}{r^2}\right)\omega_r - \frac{2}{r^2}\frac{\partial \omega_\theta}{\partial \theta}\right), \tag{2.11}$$

$$\frac{\partial \omega_\theta}{\partial t} + \frac{\partial N_r}{\partial z} - \frac{\partial N_z}{\partial r} + \frac{2}{Re}\left(\omega_r - \frac{1}{r}\frac{\partial u_z}{\partial \theta}\right) = \frac{1}{Re}\left(\left(\nabla^2 - \frac{1}{r^2}\right)\omega_\theta + \frac{2}{r^2}\frac{\partial \omega_r}{\partial \theta}\right), \tag{2.12}$$

$$\nabla^2 u_z = \frac{1}{r}\left(\frac{\partial \omega_r}{\partial \theta} - \frac{\partial (r\omega_\theta)}{\partial r}\right), \tag{2.13}$$

where

$$\nabla^2 f = \frac{\partial^2 f}{\partial r^2} + \frac{1}{r}\frac{\partial f}{\partial r} - \frac{n^2}{r^2} f + \frac{\partial^2 f}{\partial z^2}, \tag{2.14}$$

and

$$\boldsymbol{N} = (N_r, N_\theta, N_z) = \boldsymbol{\Omega}_B \times \boldsymbol{u} + \boldsymbol{\omega} \times \boldsymbol{U}_B. \tag{2.15}$$

The convective quantity $\boldsymbol{N}$ can only be evaluated if the remaining perturbation components $\{u_r, u_\theta, \omega_z\}$ are known. These so-called secondary variables are explicitly defined in terms of the primary variables by a process of integration across the boundary layer, with respect to the normal coordinate z. (More details can be found in Davies & Carpenter 2001, 2003.)

The linearization permits the no-slip conditions and the wall-normal velocity matching condition at the disk surface to be formulated as

$$u_r = -\frac{r}{Re}F'(0)\eta, \tag{2.16}$$

$$u_\theta = -\frac{r}{Re}G'(0)\eta, \tag{2.17}$$

$$u_z = \frac{\partial \eta}{\partial t}. \tag{2.18}$$

Here η is a non-dimensional vertical wall displacement that may be prescribed to impulsively generate disturbances at the disk surface. It vanishes at all radial locations once the impulse has been applied. The conditions stated in (2.16)–(2.18) are all applied at $z = 0$. Substituting the first two of them into the definitions that are used for the secondary variables u_r and u_θ gives fully equivalent integral conditions that can be used to constrain the development of the primary variables ω_θ and ω_r, respectively. (Further details can again be found in Davies & Carpenter 2001, 2003.) The condition stated in (2.18) is applied as a constraint on the remaining primary variable, u_z.

As remarked upon previously in the introduction, the linearity of the governing equations and the azimuthal symmetry of the base flow enable us to consider modes of the form

$$\{\boldsymbol{u}, \boldsymbol{\omega}\} = \{\hat{\boldsymbol{u}}, \hat{\boldsymbol{\omega}}\}\mathrm{e}^{\mathrm{i}n\theta}, \tag{2.19}$$

where n is the azimuthal mode number. Because of the circumferential periodicity of the disk, n can only take integer values. The scaled azimuthal wavenumber defined by $\beta = n/Re$ has been more usually employed by previous investigators, since for studies of the radially homogeneous version of the linear stability problem, β can be more conveniently taken to have a continuous set of values.

The methods adopted for discretization of the governing equations are discussed in detail by Davies & Carpenter (2001). A fourth-order centred, compact finite-difference scheme is used for discretization in the radial direction, whilst a Chebyshev spectral series expansion is used in the wall-normal direction, in conjunction with a mapping of the semi-infinite range of the wall-normal coordinate onto a finite interval. The azimuthal variation is imposed for each decoupled azimuthal mode number n using (2.19). A semi-implicit time advancement scheme is deployed for the vorticity transport equations, with the wall-normal second derivatives in the viscous term treated in an implicit fashion. Thomas (2007) documents the careful validation that was undertaken in order to establish that the results obtained from the numerical simulations remained valid when the effects of disk surface mass transfer were introduced into the computer code that had been developed previously for the rotating-disk boundary layer.

3. Numerical simulation results

In all of the simulations, we considered the development of disturbances that were excited by an impulsive wall motion. The wall displacement η was taken to be of the

general form

$$\eta(r, \theta\, z) = f(r - r_e)\, g(t)\, \mathrm{e}^{\mathrm{i}n\theta}, \tag{3.1}$$

where the function f is taken to be zero except within a small neighbourhood of the radial position r_e at which the impulse is centred. The temporal variation of the impulse was prescribed by setting

$$g(t) = (1 - \mathrm{e}^{-\sigma t^2})\, \mathrm{e}^{-\sigma t^2}, \tag{3.2}$$

where the parameter σ, which fixes the impulse duration, is chosen to be large enough to ensure that the initial forcing incorporates a wide range of temporal frequencies.

3.1. *Uniform mass injection*

Figure 3 displays the temporal development, at four successive radial locations, for a disturbance excited by an impulse centred at $r_e = 202$, with an azimuthal mode number $n = 29$ and $\boldsymbol{a} = -1$. The radial position of the forcing corresponds to the critical Reynolds number for the onset of absolute instability, as found by Lingwood (1997) in her stability study that employed a radial homogenization of the basic flow. The results are from a numerical simulation that was conducted for the genuine radially dependent base flow. The azimuthal vorticity ω_θ at the disk surface is plotted for a fixed value of θ, along with the corresponding envelopes $\pm|\omega_\theta|$ obtained from the complex-valued amplitude. (Similar plots are obtained when other perturbation flow variables are chosen.) Instants of time are referenced with respect to the non-dimensional time period of the disk rotation, $T = 2\pi Re$. For the radial positions $r = r_e - 25$, r_e, the disturbance decays with time, whereas for the locations $r = r_e + 25$, $r_e + 50$, there is initially a period of growth, which is followed by a relatively weak decay. It is evident that the perturbations exhibit strong spatial growth along the radial direction, when account is taken of the different scales used for the vertical axis in each of the time-history plots.

Figure 4(*a*) displays the spatial–temporal disturbance development that was obtained from the same simulation, while figure 4(*b*) displays the corresponding wavepacket when the base flow has been radially homogenized, with the Reynolds number chosen such that $Re = r_e = 202$. The disturbance development is plotted using amplitude contours of the same flow variable that was considered before, namely the azimuthal perturbation vorticity at the disk surface. The leading and trailing edges of both disturbance wavepackets are easily identified. Each of the leading edges propagates radially outwards with approximately the same non-zero velocity. However, the behaviours displayed by the trailing edges are noticeably different. The trailing edge corresponding to the homogenized-flow disturbance propagates with a diminishing velocity, which is what would be anticipated for a case where the Reynolds number has been set to be critical for the onset of absolute instability. In contrast, the trailing edge of the disturbance in the genuine flow is found to propagate radially outwards with an increasingly positive velocity.

Temporal frequencies and growth rates for the disturbance may be examined by considering the complex-valued quantity

$$\omega = \mathrm{i}\frac{1}{A}\frac{\partial A}{\partial t}, \tag{3.3}$$

where A is taken to be a measure of the disturbance amplitude at any given radial location and point in time. (The azimuthal vorticity at the disk surface was once more chosen as the representative flow variable to specify A.) It should be noted that

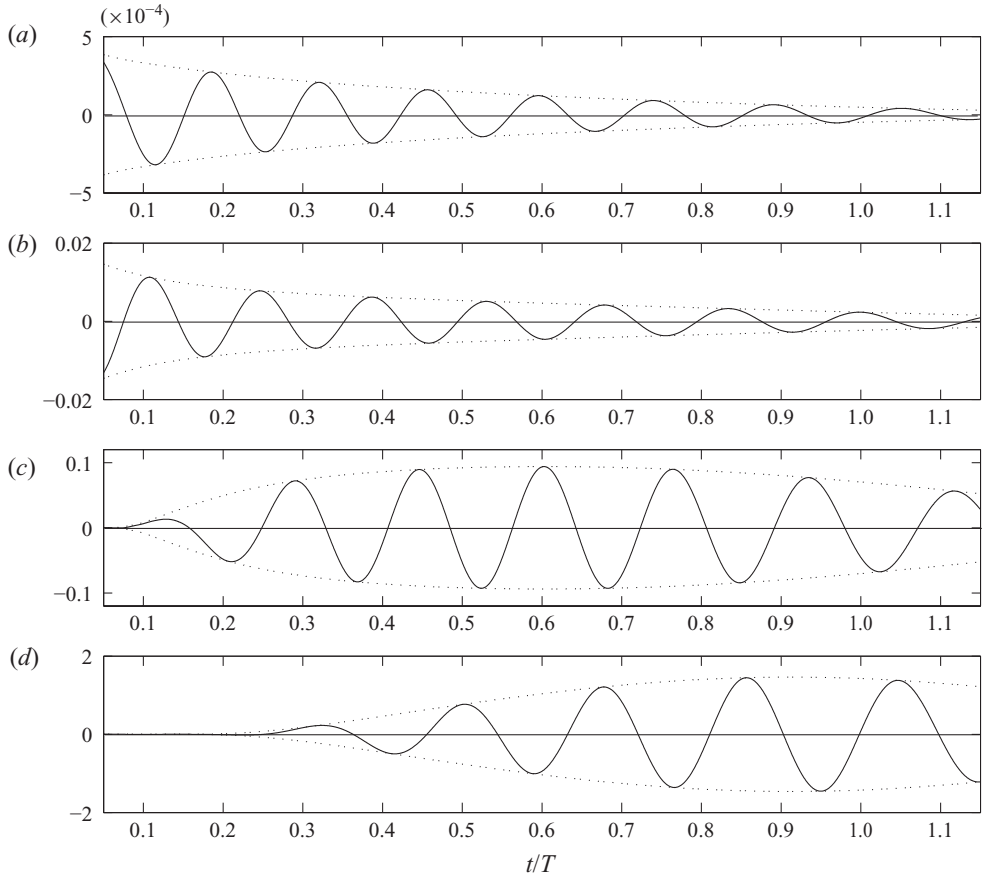

FIGURE 3. Time histories for ω_θ at the disk surface (solid lines) with corresponding envelopes $\pm|\omega_\theta|$ (dotted lines), for an impulsively excited disturbance for the radially inhomogeneous base flow with mass injection $\boldsymbol{a} = -1$. The azimuthal mode number is $n = 29$ and the disturbance was centred at $r_e = 202$. The temporal development is plotted for four successive radial locations: (*a*) $r_e - 25$, (*b*) r_e, (*c*) $r_e + 25$ and (*d*) $r_e + 50$.

we have defined the quantity ω by setting $\omega = \mathrm{i}\rho$, where ρ is the logarithmic time derivative of the amplitude A. If ω is found not to vary too rapidly in either the radial direction or in time, then the real and imaginary parts of ω may be interpreted as being locally defined temporal frequencies and temporal growth rates, respectively. Here we have assumed that the disturbance does not consist of a superposition of a number of distinct modes with significantly different characteristics. If there were, in fact, several discrete modes to consider, then it would not be feasible to identify any temporal frequency or growth rate, by simply considering the real and imaginary parts of ω.

Figure 5 displays locally defined temporal frequencies and growth rates obtained from the homogenized flow simulation. Data are given for the radial position $r_e = 202$, where the disturbance excitation was centred, and for three additional radial locations. The frequency is constant at the radial position $r_e = 202$, while the frequency at all other positions is found to asymptote towards the same constant. This behaviour is to be expected, since in the homogenized flow all radial positions are equivalent to each

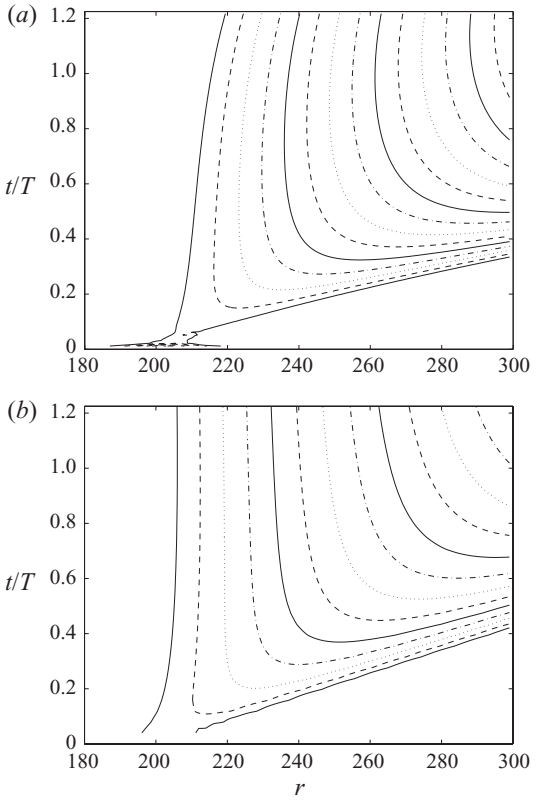

FIGURE 4. Spatio-temporal development of $|\omega_\theta|$ at the disk surface, for disturbances in flows with injection $\boldsymbol{a} = -1$. The azimuthal mode number is $n = 29$ and the disturbances were excited at $r_e = 202$. (*a*) Radially inhomogeneous base flow and (*b*) homogenized base flow with $Re = 202$. (Contours are drawn using a logarithmic scale, with levels separated by factors of two.)

other. A similar form of development is observed for the growth rates. For all the selected radial positions, the growth rates also tend to a constant. The value of this constant is approximately zero, which is consistent with the fact that the simulation has been conducted at the critical Reynolds number for the appearance of absolute instability.

The corresponding temporal frequencies and growth rates obtained from the simulation for the genuine base flow are plotted in figure 6. The behaviour is qualitatively the same as that found by Davies & Carpenter (2003). The temporal frequencies initially evolve in the manner that is observed in the homogenized-flow simulation. However, the frequency at each selected radial location then begins to increase and there is no indication that any of them will asymptote towards a constant. The associated temporal growth rates are found to decrease with time and, for all the selected radial positions, temporal decay eventually sets in; the long-term growth rates are negative. (We shall show in § 4 that the behaviour of the temporal frequencies and growth rates can be comprehended by making comparisons with solutions of the linearized Ginzburg–Landau equation.)

The numerical simulation results indicate that the disturbance evolution for the case of the flow with mass transfer $\boldsymbol{a} = -1$ remains very similar to that found

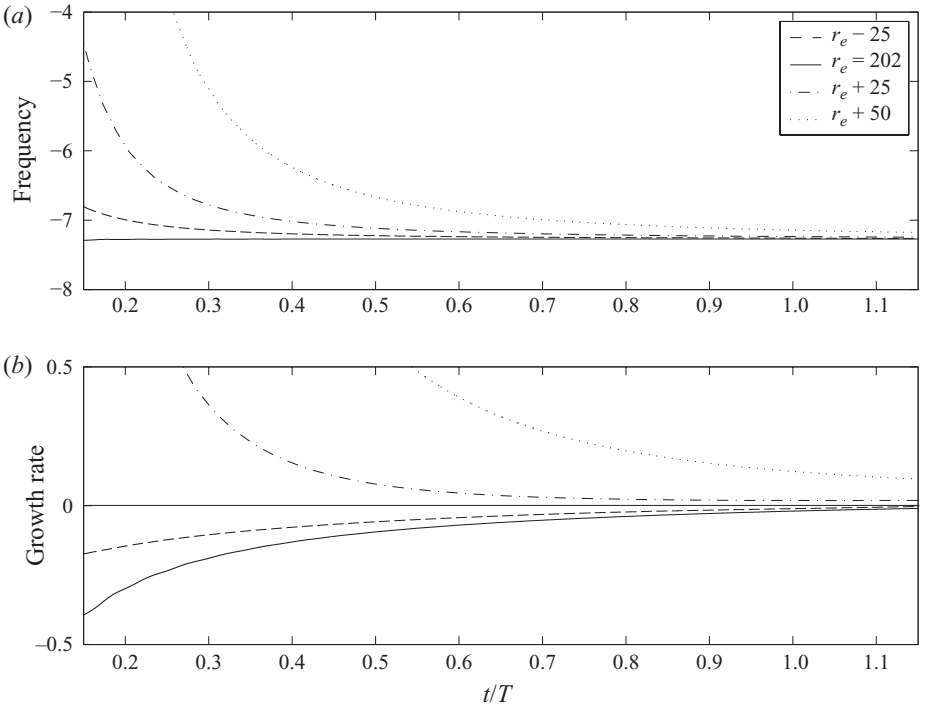

FIGURE 5. (*a*) Local temporal frequencies $\omega_r Re$ and (*b*) temporal growth rates $\omega_i Re$ for a disturbance with $n = 29$ developing in the radially homogenized flow with injection $a = -1$ and $Re = 202$. The impulsive excitation was centred at the radius labelled as $r_e = 202$. (However, note that all radial positions are effectively the same in the homogenized version of the base flow, so this labelling is only used in order to facilitate comparisons with the behaviour found in the genuine flow.) The temporal development is plotted for four different radial positions: $r_e - 25$, r_e, $r_e + 25$ and $r_e + 50$.

by Davies & Carpenter (2003) for the rotating-disk boundary layer without mass transfer. The long-term global behaviour is consistent with convective instability and does not provide any evidence to suggest the presence of an amplified linear global mode with the kind of time dependency indicated by (1.2). Disturbances continue to convect radially outwards, even when they have passed into the region of absolute instability.

A further numerical simulation was conducted in order to check the robustness of the behaviour that was found when the impulsive excitation was centred at a radius matched to the critical Reynolds number for the onset of absolute instability. The forcing was shifted radially outwards, so that the disturbance was now excited at the radial location $r_e = 302$, for the same azimuthal mode number $n = 29$ as before. This corresponds to a locally defined Reynolds number that is approximately 50 % greater than the critical value for absolute instability. The simulation results for the temporal frequencies and growth rates are plotted in figure 7. The additional solid dotted lines represent the development, at the radius where the impulse was centred, which was obtained from the corresponding homogenized-flow simulation. As before, the frequencies and growth rates, respectively, increase and decrease with time for the disturbance in the radially inhomogeneous base flow. Although temporal decay is not

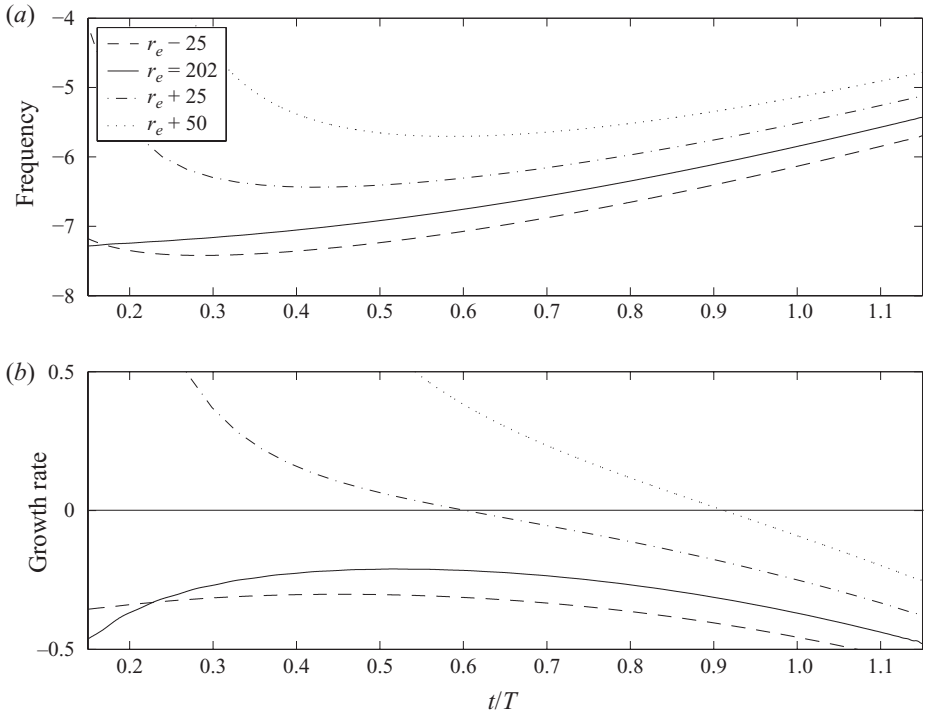

FIGURE 6. (*a*) Local temporal frequencies $\omega_r Re$ and (*b*) temporal growth rates $\omega_i Re$ for a disturbance with $n = 29$ developing in the radially inhomogeneous base flow with injection $\boldsymbol{a} = -1$. The impulsive excitation was centred at $r_e = 202$. The temporal development is plotted for four different radial positions: $r_e - 25$, r_e, $r_e + 25$ and $r_e + 50$.

observed during the time interval considered, the plots suggest that, given sufficient time, the growth rates will continually decrease until they become negative. Hence, it seems reasonable to conjecture that temporal decay will eventually set in.

Longer-duration simulations, which may have confirmed this conjecture, were extremely difficult to conduct. As in the previous study of Davies & Carpenter (2003), numerical convergence problems were encountered with the iteration scheme used to solve the discretized governing equations. The problems were due to the huge spatial variation in the disturbance magnitudes that developed within the computational domain as the disturbance wavepacket evolved. Since there is obviously no nonlinearity in governing equations that have been deliberately linearized, there are no nonlinear effects that could serve to saturate the growth. This means that the maximum amplitude of the disturbance wavepacket is allowed to grow exponentially without limit. Thus, it proved very difficult to increase the time duration of the simulations beyond that which is displayed in the figures, even by as much as only a quarter of a disk rotation period. However, in a number of closely related simulations that were conducted using various alterations in the set of parameters that specified the disturbance, the growth rates were also found to decrease. So it seems reasonable to surmise that temporal decay is likely to be the typical behaviour that will eventually be observed, for all radial locations, at least within the imposed linear framework.

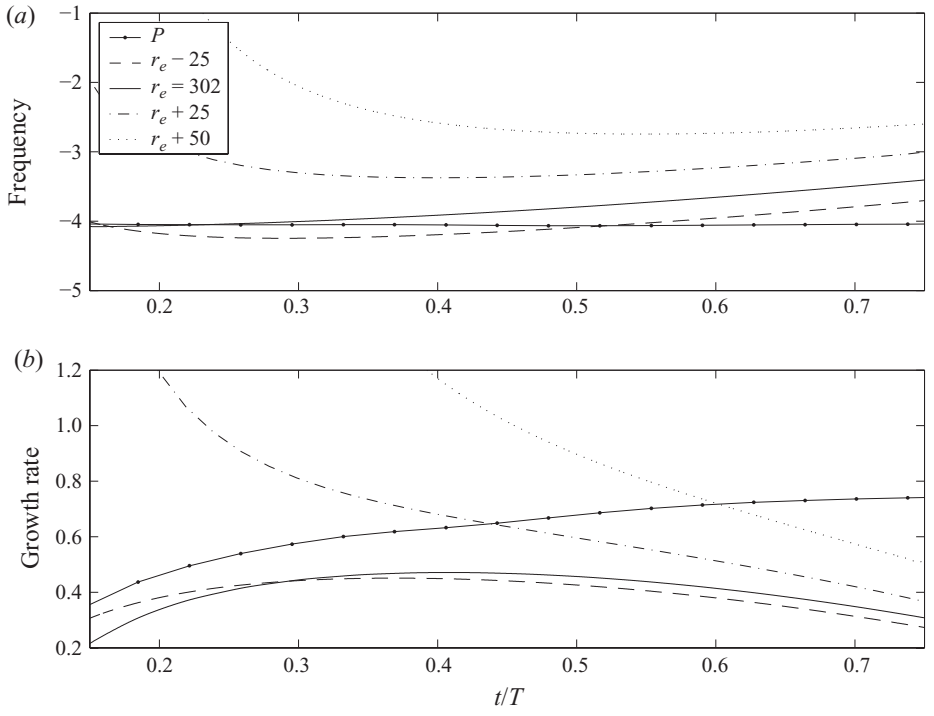

FIGURE 7. (*a*) Local temporal frequencies $\omega_r Re$ and (*b*) temporal growth rates $\omega_i Re$ for a disturbance with $n = 29$ developing in the radially inhomogeneous flow with injection $\boldsymbol{a} = -1$. The impulsive excitation was centred at $r_e = 302$. The temporal development is plotted for four different radial positions: $r_e - 25$, r_e, $r_e + 25$ and $r_e + 50$. The lines labelled as P show the development at the point of impulsive excitation for a similar disturbance in the homogenized version of the flow with $Re = 302$.

3.2. *Uniform mass suction*

We now consider disturbances developing in a base flow where the mass transfer parameter is $\boldsymbol{a} = 1$. This represents a level of suction at the disk surface that has the same strength, though oppositely directed, as the injection case that was considered in the previous section. Figure 8 displays the temporal development, at four successive radial positions, in the radially inhomogeneous flow for a disturbance with an azimuthal mode number $n = 194$ that was excited by an impulse centred at $r_e = 1861$. The azimuthal mode number and radial position of the impulse specify the conditions for critical absolute instability, as determined by Lingwood (1997). For the radial positions $r_e - 25$, r_e it can be seen that the disturbance initially decays, but then appears to asymptote towards a constant amplitude. Radially outboard from the impulse position, at the locations $r_e + 25$, $r_e + 50$, the disturbance exhibits temporal growth that accumulates over the time interval considered, though at the first of these two chosen locations there is also a prolonged period during which the amplitude remains approximately constant.

The spatial–temporal development of the disturbance is displayed in figure 9(*a*). At first glance, the behaviour appears to be in precise accordance with what might reasonably be anticipated for an impulse that is centred at the radius that corresponds to the critical Reynolds number for absolute instability; the leading edge propagates radially outwards with a non-vanishing velocity, while the trailing edge seems to

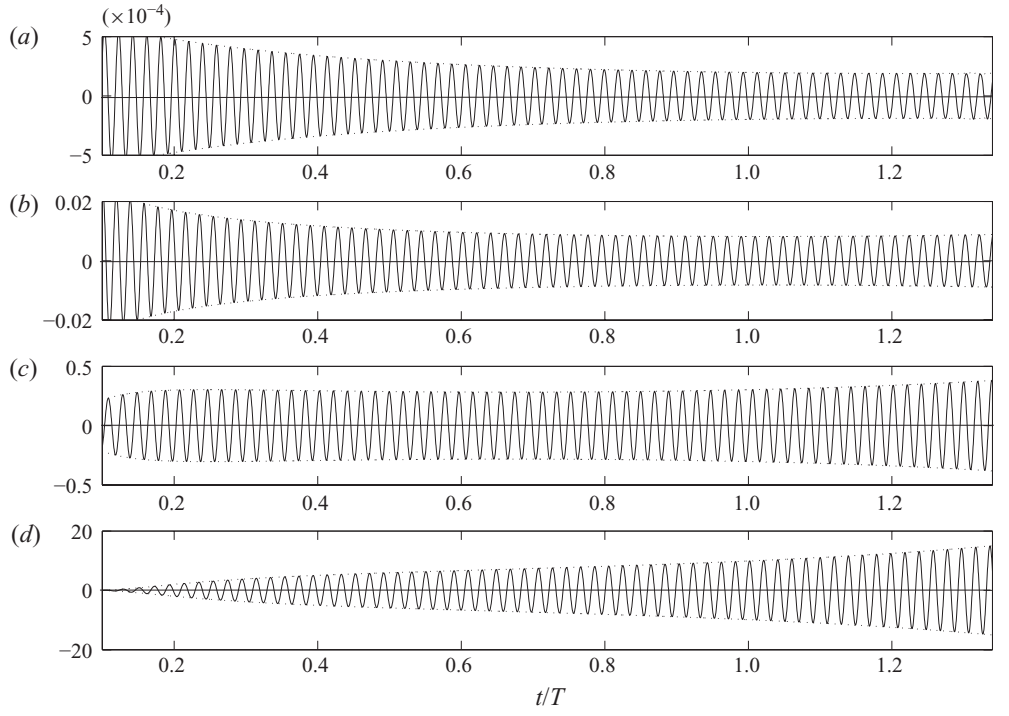

FIGURE 8. Time histories for ω_θ at the disk surface (solid lines) with corresponding envelopes $\pm|\omega_\theta|$ (dotted lines), for an impulsively excited disturbance in the radially inhomogeneous base flow with suction $\boldsymbol{a} = 1$. The azimuthal mode number is $n = 194$ and the disturbance was excited at $r_e = 1861$. The temporal development is plotted for four different radial positions: (*a*) $r_e - 25$, (*b*) r_e, (*c*) $r_e + 25$ and (*d*) $r_e + 50$.

propagate with a near-zero velocity. However, on closer inspection, it may be seen that the trailing edge eventually moves radially inwards with a small, but growing velocity. This is illustrated in figure 9(*b*), where a more limited range of radial positions is considered in the vicinity of the trailing edge. Thus, the long-term development seems to be different from what was found for the case with mass injection, where the behaviour had remained similar to that described by Davies & Carpenter (2003) for the rotating disk flow with no mass transfer.

Figure 10 displays the temporal development of the locally defined temporal frequencies and growth rates for the disturbance. Results are again plotted for four separate radial positions. (The solid dotted lines, labelled as *P*, refer to the corresponding homogenized-flow simulation, where the Reynolds number is $Re = 1861$.) The frequencies behave in a manner that is very much the same as reported earlier, for the flow with mass injection; they increase at later times and vary systematically with the radius. However, the temporal growth rates behave rather differently. They are displayed over the full time interval of the numerical simulation in figure 10(*b*), and for a reduced range of time in figure 10(*c*). At all of the selected radial locations, the growth rates are increasing, either for the whole of the time interval considered or during its latter part. Temporal growth is eventually observed at every one of the chosen positions, represented by positive values of the growth rates. It is not possible to entirely discount the prospect that the increasing trend of the growth rates might be reversed at later times, by just considering the results of a

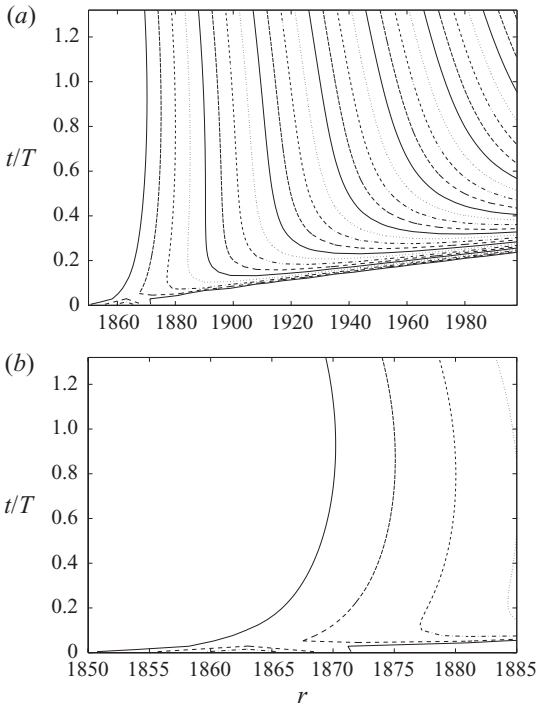

FIGURE 9. Spatio-temporal development of $|\omega_\theta|$ at the disk surface for an impulsively excited disturbance in the radially inhomogeneous flow with suction $\boldsymbol{a} = 1$. The azimuthal mode number is $n = 194$ and the disturbance was excited at $r_e = 1861$. (*a*) Full radial range and (*b*) reduced radial range around the trailing edge.

simulation that could only be conducted over a relatively short time interval of less than one and a half disk rotation periods. Nevertheless, the new behaviour that is displayed in the growth rates suggests the presence of some form of global instability, albeit without the selection of any dominant global frequency, as would usually be anticipated.

In a further simulation, a disturbance was excited radially inwards from the location predicted for the onset of absolute instability by a homogenized-flow analysis. The impulse used to trigger the disturbance was now centred at $r_e = 1811$, rather than at $r_e = 1861$, with the same azimuthal mode number, $n = 194$, as before. Figure 11 displays the spatial–temporal development. The trailing edge of the disturbance wavepacket propagates radially outwards, but it moves more and more slowly as it approaches the absolutely unstable region. The contour that represents the trailing edge appears to turn towards being vertical in the spatial–temporal plot, as it nears the location $r_c = 1861$ that corresponds to critical absolute instability.

Figure 12 displays the local temporal frequencies and growth rates at the radial locations $r_e = 1811$, $r_e + 25$, $r_e + 50$ and $r_e + 100$ for the same disturbance as above. (The frequency and growth rate for the corresponding homogenized-flow simulation, with $Re = 1811$, are also included in the figure; labelled P as before.) It can be seen that for the innermost three of the chosen radial positions, where $r \leqslant r_c = r_e + 50$, there is a prolonged period of temporal decay. However, the trend of the growth rates suggests that this does not persist indefinitely. There is a good indication that the growth rates will eventually become positive at all of

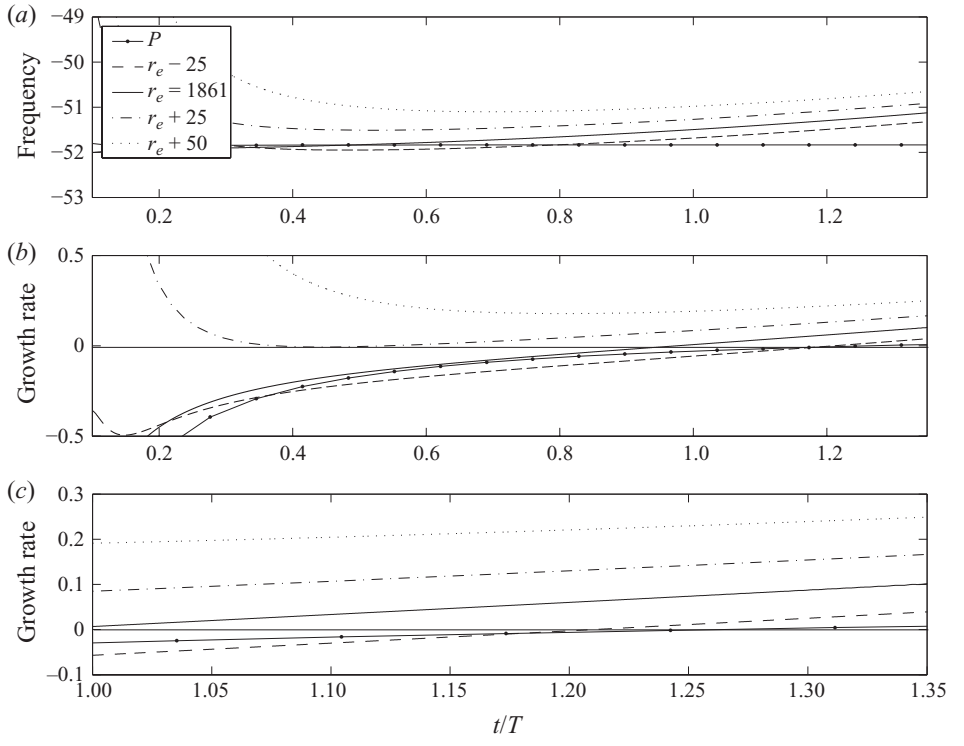

FIGURE 10. (*a*) Local temporal frequencies $\omega_r Re$ and (*b*,*c*) temporal growth rates $\omega_i Re$ for a disturbance with $n = 194$ developing in the radially inhomogeneous flow with suction $\boldsymbol{a} = 1$, centred at $r_e = 1861$. The temporal development is plotted for four different radial positions: $r_e - 25$, r_e, $r_e + 25$ and $r_e + 50$. The solid dotted lines labelled with a P show the development in the corresponding homogenized flow with $Re = 1861$. The temporal growth rates are displayed over the full time interval in (*b*) and for a reduced range of later times in (*c*).

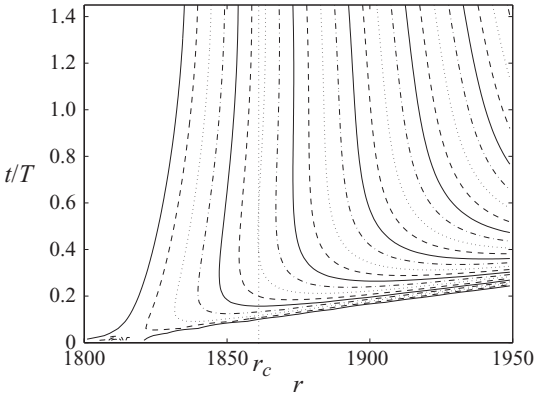

FIGURE 11. Spatio-temporal development of $|\omega_{\theta,w}|$ at the disk surface for an impulsively excited disturbance in a radially inhomogeneous flow with suction $\boldsymbol{a} = 1$. The azimuthal mode number is $n = 194$ and the disturbance was excited at $r_e = 1811$. The vertical line at r_c represents the critical radius for the onset of absolute instability.

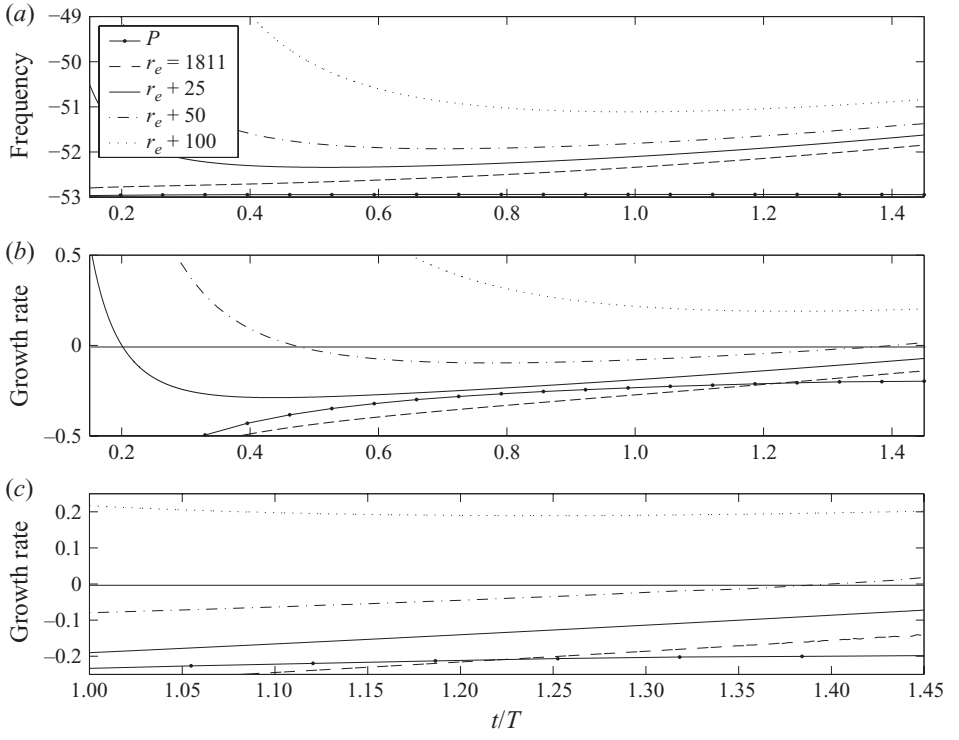

FIGURE 12. (*a*) Local temporal frequencies $\omega_r Re$ and (*b*,*c*) growth rates $\omega_i Re$ for a disturbance with $n = 194$ developing in the radially inhomogeneous flow with suction $\boldsymbol{a} = 1$. The impulse was centred at $r_e = 1811$. The temporal development is plotted for four different radial positions, r_e, $r_e + 25$, $r_e + 50$ and $r_e + 100$. The solid dotted lines labelled with a P show the development in a homogenized flow with $Re = 1811$. The temporal growth rates are displayed over a full time range in (*b*) and for a reduced range of later times in (*c*).

the radial positions displayed. However, be that as it may, it should be observed that for $r = r_e + 50$, temporal growth is certainly in evidence after $t/T = 1.4$, which is just before the end of the time interval considered. There is also temporal growth at $r = r_e + 100$ throughout the whole duration of the simulation. A similar exhibition of temporally growing behaviour was found for other radial locations where $r > 1861$, with the locally defined growth rates becoming more pronounced as the radius increased. Thus, even though the time allowed for the disturbance evolution was constrained by the limitations of the numerical simulation, which meant that the appearance of positive growth rates could not be confirmed at radial locations where $r < 1861$, the overall behaviour seems to again signal the presence of a global instability.

An additional illustration of the differences between the rotating-disk flows with mass injection and suction can be obtained by comparing the behaviour of disturbances that are impulsively excited at a location that is far away from the radius that marks the boundary for the onset of absolute instability, but is still within the region of convective instability. Figure 13(*a*) displays the spatial–temporal development of a disturbance wavepacket excited at $r_e = 712$ with $n = 113$ in a flow with suction of strength $\boldsymbol{a} = 0.5$. Radially homogenized-flow analysis predicts that the onset of absolute instability will occur at the radial location $r_c = 912$,

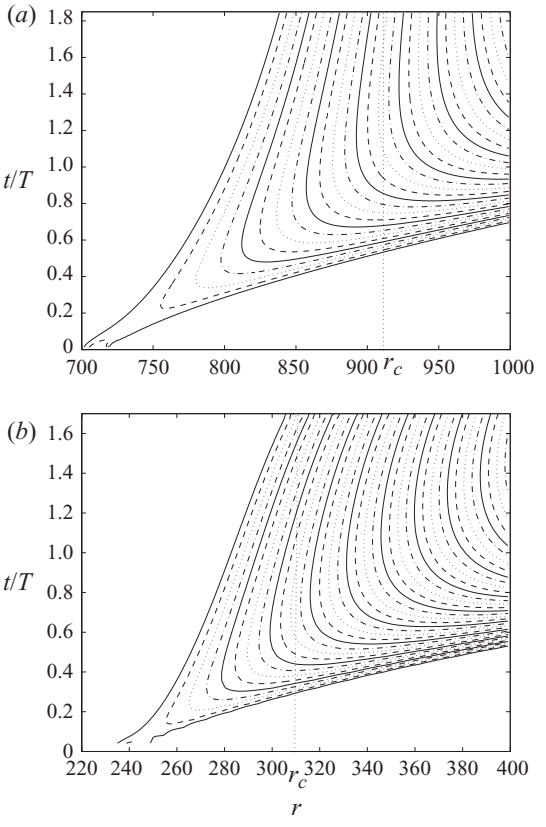

FIGURE 13. Spatio-temporal development of $|\omega_\theta|$ at the disk surface for an impulsively excited disturbance in radially inhomogeneous flows. A dotted vertical line at the radius r_c marks the position for the onset of absolute instability that is predicted using homogenized-flow analysis. (*a*) $\boldsymbol{a} = 0.5$ for an azimuthal mode number $n = 113$ excited at $r_e = 712$ ($r_c = 912$); (*b*) $\boldsymbol{a} = -0.5$ for an azimuthal mode number $n = 43$ excited at $r_e = 240$ ($r_c = 310$).

for the stated azimuthal wavenumber. Figure 13(*b*) shows the spatial–temporal development for an injection flow with $\boldsymbol{a} = -0.5$. The disturbance is excited at $r_e = 240$, whilst absolute instability sets in at $r_c = 310$, for the chosen wavenumber $n = 43$. A significant contrast between the behaviours in the two flows can be seen immediately. The trailing edge of the disturbance wavepacket for $\boldsymbol{a} = 0.5$ propagates with a diminishing velocity as it moves radially outwards, while for $\boldsymbol{a} = -0.5$ the trailing edge progresses with an increasing propagation velocity, which should carry it beyond the radial position where absolute instability is predicted to appear.

3.3. *Comparison of temporal growth rates for flows with different mass transfer*

A number of rotating-disk flows with various degrees of mass transfer were investigated in order to systematically trace the changes in behaviour between flows with suction and those with injection. Figure 14 provides a convenient means of highlighting these changes. It compares the growth rates of disturbances that were excited at the radius corresponding to the critical point for absolute instability, for five flows with different levels of mass transfer $\boldsymbol{a} = -1, -0.5, 0, 0.5, 1$. Initially,

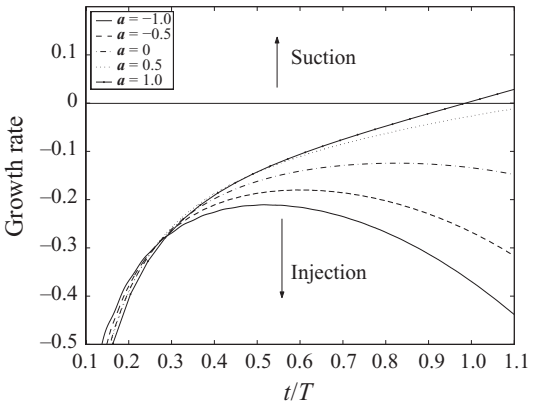

FIGURE 14. Growth rates for a disturbance excited at the radius $r = r_c$ corresponding to the onset of absolute instability for the rotating disk flows with various degrees of mass transfer. Solid line, $\boldsymbol{a} = -1$ where $r_c = 202$, $n = 29$; dashed line, $\boldsymbol{a} = -0.5$ where $r_c = 310$, $n = 43$; dash-dotted line, $\boldsymbol{a} = 0.0$ where $r_c = 508$, $n = 67$; dotted line, $\boldsymbol{a} = 0.5$ where $r_c = 912$, $n = 113$; solid dotted line, $\boldsymbol{a} = 1$ where $r_e = 1861$, $n = 194$.

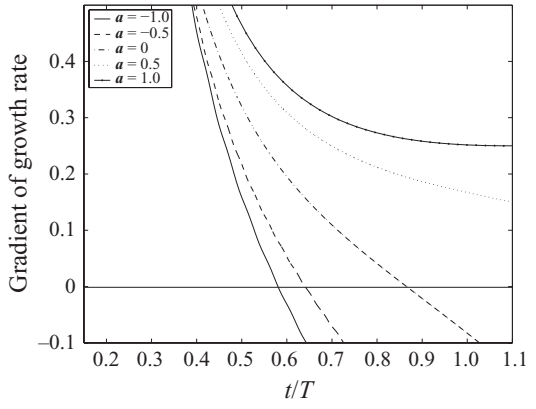

FIGURE 15. Gradients of the growth rates in figure 14. Data lines are for the same parameters as before.

the behaviour displayed in all five of the plots is similar; the growth rates begin with commensurate negative values and then increase rapidly. However, after a time interval of only $t/T = 0.4$, noticeable differences in the growth rates start to emerge. The increases in the growth rates that correspond to the flows with $\boldsymbol{a} \leqslant 0$ become less rapid, until they are eventually reversed and replaced by a decrease. In contrast, the growth rates for the suction flows with $\boldsymbol{a} > 0$ continue to increase, although this increase is far weaker than it was initially. By the end of time interval considered, the growth rate for the case $\boldsymbol{a} = 1$ has become positive, while the growth rate for $\boldsymbol{a} = 0.5$ has a trend that suggests that it will also become positive, but at a slightly later time.

Figure 15 displays the gradients of the growth rates that were shown in figure 14. The data lines are for exactly the same parameters as before. For $\boldsymbol{a} \leqslant 0$ the gradients diminish and eventually become negative, which corresponds to the growth rates decreasing. For $\boldsymbol{a} = 0.5$ the gradient remains positive for the whole of the time period displayed. However, the gradient continues to decrease and it is not clear

whether or not it will asymptote to a positive-valued constant. If it does, then the long-term behaviour will be the same as that for the case $\boldsymbol{a} = 1$ which is described below. If the gradient for $\boldsymbol{a} = 0.5$ does not asymptote to a positive constant, then the corresponding growth rate can be expected to decrease until it becomes and remains negative, even though it may be positive for a lengthy intervening time interval. Thus, it is not possible to entirely discount the possibility of a long-term temporal decay of the disturbance. The behaviour for $\boldsymbol{a} = 1$ seems much clearer. The gradient of the growth rate initially decreases, but then there is a very strong suggestion that it may asymptote towards a positive constant, or perhaps even begin to increase again. The trend of the gradient thus indicates that the long-term disturbance behaviour will consist of temporal growth with an increasingly large growth rate. Such disturbance growth signifies the presence of global instability, though the time dependence is evidently far more complicated than that which would be associated with a global mode of the form (1.2); there is no selection of a global temporal growth rate, in addition to the previously noted absence of any selected global frequency.

4. Modelling using the Ginzburg–Landau equation

For the rotating-disk boundary layer with mass injection applied at the disk surface, there would seem to be a disparity between the radially increasing strength of the absolute instability and the absence of any obvious signs of global instability in the numerical simulation results. It is not immediately evident how it could be possible to resolve this apparent conflict between the local instability properties, deduced using the approximation of a radially homogenized flow, and the global stability that is presented in the simulations for the genuine inhomogeneous flow. An initial impression might be given that there is something amiss in either the absolute stability analysis or the numerical simulations. Fortunately, some insight can be gained by considering analogous behaviour that occurs in impulse solutions of the linearized complex Ginzburg–Landau equation (Hunt & Crighton 1991). This kind of modelling was first utilized by Davies *et al.* (2007) to provide a theoretical explanation of the numerical simulation results that were obtained by Davies & Carpenter (2003) for the rotating disk boundary layer with no mass transfer. In this study, we consider an extension of the same approach to cases where there is mass transfer at the disk surface. We shall show that the model impulse solutions encompass a range of behaviour that includes the novel form of global instability that is displayed in the simulations with suction, as well as the global stability that is found when there is mass injection.

4.1. *Impulse solutions*

The linearized Ginzburg–Landau equation may be written in the form:

$$\frac{\partial \psi}{\partial t} + U\frac{\partial \psi}{\partial r} = \mu\psi + \gamma\frac{\partial^2 \psi}{\partial r^2}, \tag{4.1}$$

where $\psi(r, t)$ is some measure of the disturbance amplitude at the radial location r and time t. The terms multiplied by the quantities μ, U and γ (where $\mathrm{Re}(\gamma) > 0$) are used, respectively, to model the effects of temporal growth/oscillation, flow convection and diffusion/dispersion. Usually, all three of these quantities are taken to be constant, in order to provide a model for the development of disturbances in a spatially homogeneous flow. However, by setting $\mu = \mu(r)$ we can obtain a simple, if somewhat crude, model for disturbances that evolve in a flow that is spatially inhomogeneous.

At any given location, the real part of the derivative $\mathrm{d}\mu/\mathrm{d}r$ can be interpreted as a local measure of the radial variation in the temporal stability properties of the flow. The imaginary part of $\mathrm{d}\mu/\mathrm{d}r$ quantifies the corresponding spatial dependency in the temporal frequencies at which disturbances can be excited.

The simplest non-trivial radial variation in μ that may be considered is the case where $\mathrm{d}\mu/\mathrm{d}r$ is prescribed to be a constant μ_1, so that we have the linear dependency

$$\mu = \mu_0 + \mu_1 r, \tag{4.2}$$

with μ_0 as another constant. For this form of μ, the Green function $G(r, t)$ solution of the Ginzburg–Landau equation (4.1) can be shown to be (Hunt & Crighton 1991)

$$G(r,t) = \sqrt{\frac{1}{4\pi\gamma t}} \exp\left(\mu_0 t - \frac{(r-Ut)^2}{4\gamma t} + \frac{1}{2}\mu_1 r t + \frac{1}{12}\mu_1^2 \gamma t^3\right). \tag{4.3}$$

This represents the response to a localized impulse $\sim \delta(t)\,\delta(r)$. (For convenience, we consider an impulse centred at $r = 0$. The impulse location can be translated to $r = r_e$ when comparisons are made with numerical simulation results.) Identifying the instantaneous complex growth rate of a disturbance with the logarithmic derivative

$$\rho = \frac{1}{G}\frac{\partial G}{\partial t}, \tag{4.4}$$

it may easily be seen that, for large times, the impulsively excited disturbance grows at a rate

$$\mathrm{Re}(\rho) \sim \tfrac{1}{4}\left[(\mu_{1r}^2 - \mu_{1i}^2)\gamma_r - 2\mu_{1r}\mu_{1i}\gamma_i\right]t^2, \tag{4.5}$$

where μ_{1r} and μ_{1i} denote the real and imaginary parts of μ_1, respectively, and similarly for γ. Using the fact that $\gamma_r > 0$, it may be deduced that when the measure of the frequency variation μ_{1i} is large enough in magnitude, there is a globally stable response. (More precise details of the conditions necessary for global stability are given below.) This can happen even if μ_{1r} is positive, which would correspond to a flow that becomes locally more and more unstable as the radius increases. Thus, the behaviour of the impulse solution (4.3) indicates how detuning, arising from the spatial variation of the temporal frequency of an absolute instability, may be sufficient to globally stabilize disturbances. It provides a possible explanation of why an absolutely unstable rotating-disk boundary-layer flow can remain globally stable. As will be seen immediately below, the appearance of global stability depends on how well the radial increases in growth rates are balanced by the corresponding shifts in frequencies. A rather different type of behaviour can be anticipated if the combination of parameters enclosed in the square brackets in (4.5) happens to be positive. It may be surmised that a novel form of global instability will then arise, with a positive growth rate $\propto t^2$ for the impulse response at large times.

For there to be a globally stable response to an impulse, more specific conditions can be obtained as follows. Let $\lambda = \mu_{1r}/\mu_{1i}$ and $\Gamma = \gamma_i/\gamma_r$. Then, from (4.5), it may be deduced that there will be global stability whenever

$$(\lambda - \Gamma)^2 - (1 + \Gamma^2) < 0. \tag{4.6}$$

Thus, globally stable behaviour prevails if

$$\Gamma - \sqrt{1+\Gamma^2} < \lambda < \Gamma + \sqrt{1+\Gamma^2}. \tag{4.7}$$

Therefore, the long time response is determined by the relative sizes of the quantities μ_{1r} and μ_{1i} that measure the radial variation in the temporal growth rates and

the temporal frequencies, respectively. There is also a dependence upon the ratio of the parameters that quantify the diffusion and dispersion effects. A simplification occurs when γ is entirely real, which represents cases where there is diffusion but no dispersion. The inequality (4.7) then reduces to $|\lambda| < 1$, that is $|\mu_{1r}| < |\mu_{1i}|$. Using the linearity relation (4.2) which is assumed for μ, this can be rewritten as

$$\left|\frac{\mathrm{d}\mu_r}{\mathrm{d}r}\right| < \left|\frac{\mathrm{d}\mu_i}{\mathrm{d}r}\right|. \tag{4.8}$$

For each of the rotating-disk boundary-layer simulations that we compared with impulse solutions of the Ginzburg–Landau equation, our numerical estimates always suggested that $|\mathrm{d}\mu_r/\mathrm{d}r| < |\mathrm{d}\mu_i/\mathrm{d}r|$. If γ were purely real, this would imply that there could only be global stability. Hence, in order to successfully model the globally unstable behaviour that was seen in simulations where disk surface suction was applied, it will be necessary to allow γ to be complex. This is in addition to taking μ_1 to be complex, so as to model the detuning effects due to the radial variation in the temporal frequency of the absolute instability. In related studies, Gajjar (1996) and Gajjar, Arebi & Sibanda (1996) examined the nonlinear development of disturbances in three-dimensional boundary layers that included rotating-disk flows. Using a high-Reynolds-number asymptotic analysis, they were able to derive a novel integro-partial differential equation. For linearized disturbances, their amplitude equation does not retain any term which corresponds to the diffusion/dispersion term that appears in the linearized Ginzburg–Landau equation. In contrast, our modelling approach suggests that the inclusion of a diffusion/dispersion term is necessary for capturing the influence of the radial inhomogeneity of the base flow.

Before turning our attention to matching the numerical simulation results to Ginzburg–Landau impulse solutions, it is worth noting that the large time behaviour of the imaginary part of the logarithmic growth rate takes the form

$$\mathrm{Im}(\rho) \sim \tfrac{1}{4}\left[\left(\mu_{1r}^2 - \mu_{1i}^2\right)\gamma_i + 2\mu_{1r}\mu_{1i}\gamma_r\right]t^2 \,. \tag{4.9}$$

This implies that in general, when μ_{1i} and γ_i are non-vanishing, there is no selection of any dominant temporal frequency in the impulse response, irrespective of whether or not there is any global instability.

4.2. *Determination of the model parameters from the simulations*

We will now describe how we were able to fit the impulse solutions (4.3) to the numerical results that were obtained from the simulations for rotating-disk boundary layers with various degrees of mass transfer. Expressions will be derived which will allow quantities that can be determined directly from the simulation data to be utilized in estimating the parameters that appear in the Ginzburg–Landau equation. Throughout this section, we shall assume that a global rather than a local form of time non-dimensionalization has been adopted. (Apart from the need to have a form of time non-dimensionalization that can be applied in a consistent manner at different radial positions in the inhomogeneous flow, the adoption of a global time scale helps to keep the notation as simple as possible. The conversion between the local and global time scales would otherwise introduce a factor of Re into various quantities, reflecting the fact that the non-dimensionalized disk rotation period is changed from $2\pi Re$ to 2π. See Davies *et al.* 2007 for a detailed discussion.)

We first note that the impulse solution (4.3) can be written in a more convenient form as

$$G(r,t) = \sqrt{\frac{1}{4\pi\gamma t}} \exp\left(-\frac{r^2}{4\gamma t} + \frac{1}{2}\mu_1 r t + \frac{1}{12}\mu_1^2 \gamma t^3\right) \exp\left(\mathrm{i}(\alpha_0 r - \omega_0 t)\right)$$

$$= G_*(r,t) \exp\left(\mathrm{i}(\alpha_0 r - \omega_0 t)\right), \tag{4.10}$$

where

$$\omega_0 = \mathrm{i}\left(\mu_0 - \frac{U^2}{4\gamma}\right), \quad \alpha_0 = -\mathrm{i}\frac{U}{2\gamma}. \tag{4.11}$$

It may easily be verified that $G_*(r,t)$ satisfies the simplified Ginzburg–Landau equation

$$\frac{\partial G_*}{\partial t} = (\mu_1 r) G_* + \gamma \frac{\partial^2 G_*}{\partial r^2}. \tag{4.12}$$

Explicit reference to the convection velocity U has been removed by the introduction of the temporal frequency ω_0 and the radial wavenumber α_0, both of which will be complex-valued in general.

As in § 3.1, we can define a local complex frequency by setting

$$\omega = \mathrm{i}\rho = \mathrm{i}\frac{1}{G}\frac{\partial G}{\partial t}. \tag{4.13}$$

Using (4.10) it may be seen that

$$\omega = \omega_0 + \mathrm{i}\left(-\frac{1}{2t} + \frac{r^2}{4\gamma t^2} + \frac{1}{2}\mu_1 r + \frac{1}{4}\mu_1^2 \gamma t^2\right). \tag{4.14}$$

In the case of a radially homogeneous flow, for which μ_1 vanishes, we have $\omega \to \omega_0$ as $t \to \infty$. Thus, ω_0 is the complex frequency that characterizes the long-term temporal behaviour of disturbances in the homogenized flow. There is absolute instability when $\mathrm{Im}(\omega_0) > 0$.

In a similar manner as for the frequency, a local complex wavenumber for the radial variation of disturbances can be defined as

$$\alpha = -\mathrm{i}\frac{1}{G}\frac{\partial G}{\partial r}. \tag{4.15}$$

The expression for the Green function (4.10) then yields

$$\alpha = \alpha_0 + \mathrm{i}\left(\frac{r}{2\gamma t} - \frac{1}{2}\mu_1 t\right). \tag{4.16}$$

So $\alpha \to \alpha_0$ for $t \to \infty$, when μ_1 is zero. This means that α_0 can be interpreted as being the complex wavenumber that is associated with disturbances in the homogeneous flow at large times.

The complex constants ω_0 and α_0 can be obtained from numerical simulations conducted for a radially homogenized rotating-disk boundary layer in a straightforward manner. They may simply be set equal to numerically determined estimates for the large time asymptotes of ω and α, where these quantities remain defined just as in (4.13) and (4.15), but with the Green function $G(r,t)$ replaced by some suitable measure of the disturbance amplitude $A(r,t)$ that is provided as data from the simulation. (Typically, the amplitude of the azimuthal vorticity perturbation at the disk surface was utilized.)

An examination of the detailed structure of the Green function (4.10), when μ_1 is zero, reveals that the disturbance wavepacket that it represents has leading and trailing edges located at $r = U_L t$ and $r = U_T t$, respectively, where the velocities U_L and U_T satisfy the following relationships:

$$\left(\frac{1}{\gamma}\right)_r = -\frac{4\alpha_{0i}}{U_L + U_T} = -\frac{4\omega_{0i}}{U_L U_T}. \tag{4.17}$$

Hence, once a value for either α_{0i} or ω_{0i} has been determined, the parameter $(1/\gamma)_r$ may, in principle, be estimated using values for the leading and trailing velocities that can be obtained from an inspection of the slopes of amplitude contour plots for the spatial–temporal development of simulated disturbance wavepackets in the homogenized flow. However, in practice, it was frequently found that $|U_T| \ll |U_L|$, which made it difficult to estimate U_T with adequate precision using contour plots. In fact, such a problem in the estimation of U_T may be anticipated from the appearance of the factor $1/\sqrt{t}$ in the impulse solution of the Ginzburg–Landau equation that we have been considering. This algebraic decay factor means that any disturbance amplitude contours that are located near the trailing edge can be expected to approach lines with slope U_T rather slowly, as time passes, whenever U_T takes a value that is relatively small. Therefore, in practice, the amplitude contour plots, which were constructed using the simulation data, could often only be deployed to estimate the value of the leading-edge velocity U_L with an acceptable degree of precision. When this was the case, the relationships stated in (4.17) were applied to determine U_T, as well as $(1/\gamma)_r$, using the values given for α_{0i}, ω_{0i} and U_L.

An estimate for the parameter γ_i also needs to be provided, so that γ can be fully specified. This can be achieved by using homogenized flow simulation data for disturbance amplitudes to compute the derivative $\partial\alpha/\partial r$, and then noting that, when μ_1 vanishes, we can derive the relationship

$$\frac{\gamma_i}{\gamma_r} = \frac{\partial\alpha_r}{\partial r} \Big/ \frac{\partial\alpha_i}{\partial r}, \tag{4.18}$$

using the expression (4.16) that holds for the impulse solution of the Ginzburg–Landau equation.

Thus far we have indicated how values for the complex parameters γ, α_0 and ω_0 may be extracted from the results of numerical simulations conducted for impulsively excited disturbances in the homogenized rotating disk flow. The final complex parameter μ_1, which is used to model the effects of the radial inhomogeneity in the genuine flow, can be determined as follows. From the expression (4.14) for the locally defined complex frequency ω, it may be seen that

$$\frac{\partial\omega}{\partial r} = \mathrm{i}\left(\frac{r}{2\gamma t^2} + \frac{1}{2}\mu_1\right), \tag{4.19}$$

and hence, $\partial\omega/\partial r \to \mathrm{i}\mu_1/2$ as $t \to \infty$. Thus, disturbance amplitude data obtained from a numerical simulation for the inhomogeneous flow can be deployed to specify a value for μ_1, by providing an estimate for the large-time asymptotic value of the radial derivative of the locally defined complex frequency. Alternatively, homogenized-flow simulations conducted for slightly different values of the Reynolds number Re can be used to determine the rate at which the asymptotic complex frequency ω_0 varies with

the Reynolds number. The parameter μ_1 can then be estimated using the relation

$$\frac{\mathrm{d}\omega_0}{\mathrm{d}Re} = \mathrm{i}\mu_1. \tag{4.20}$$

It may be observed from (4.19) and (4.20) that, for large times, the rate at which the complex frequency varies with the radius in the genuine inhomogeneous flow is anticipated to be only half the rate at which it varies with the Reynolds number amongst radially homogenized flows. However, it is only in the homogenized case that the frequency itself, rather than its radial derivative, approaches any settled value for large enough times.

4.3. *Matching with numerical simulation results*

We now present an example to illustrate the kind of matching that can be achieved between numerical simulation results and impulse solutions of the Ginzburg–Landau equation. In line with the procedure outlined above, there is a first step where simulation data obtained for the radially homogenized flow are used to estimate γ, α_0 and ω_0. Simulation data for the inhomogeneous flow, or for the homogenized flow at different Reynolds numbers, are then used to fix a value for μ_1.

Note that no optimization is attempted in the procedure used to determine the parameters that appear in the impulse solutions of the Ginzburg–Landau equation. No doubt, the degree of quantitative agreement could be improved by increasing the sophistication of the data fitting, for example by the introduction of some form of least-squares minimization of any disparities with the simulation results. However, our primary concern here is to provide a few rudimentary comparisons with the predictions of an explanatory model that has been kept as simple as possible. Strategies for obtaining an improvement in the data fit are of secondary importance. If we had so desired, the numerical accuracy of the modelling could also have been improved by increasing the underlying complexity of the Ginzburg–Landau equation. It is not very difficult to incorporate more general forms for the radial dependency of μ, and/or allow γ and U to become spatially dependent in various ways (see Hunt & Crighton 1991 and Thomas 2007 for further details). However, again for simplicity, we will not pursue such possibilities.

The particular rotating disk boundary layer that we have chosen for the purposes of illustration has mass suction with $\boldsymbol{a} = 1$. We were also able to successfully model the numerical simulation results for cases with mass injection (Thomas 2007), though the details will not be presented here. Aside from space constraints, this is because the globally stable behaviour that was found for rotating disk boundary layers with mass injection remains quite similar to that which occurs in the absence of any mass transfer. Results obtained from the modelling for the case with no mass transfer have already been described, albeit rather briefly, by Davies *et al.* (2007). Few details were given there of how the parameters used to characterize the model were estimated. Nor was there any account of the variety of global behaviour that is possible according to the model.

In our selected example with $\boldsymbol{a} = 1$, the impulse used to excite the disturbance was centred at a radius corresponding to a Reynolds number $Re = r_e = 1911$, for an azimuthal mode number $n = 194$. The Reynolds number that marks the onset of absolute instability is 1861. Thus, in the radially inhomogeneous flow, the disturbance was excited some distance outboard from the critical radius. For the homogenized version of the flow, numerical simulation results for the temporal frequencies, growth rates and spatio-temporal development of the disturbance are plotted in figures 16(*a*),

16(c) and 16(e), respectively. The complex frequency eventually asymptotes towards $\omega_0 Re \approx -51.1 + \mathrm{i}0.28$. (Note that we have now reverted to using a locally based time non-dimensionalization when specifying the frequency ω_0, which leads to the appearance of a factor Re in various quantities. Though it is only strictly appropriate to use a local time scale for the analysis of disturbances developing in the homogenized flow, we have retained its use here, and elsewhere in the paper, in accordance with the practice that has been most commonly adopted by other investigators.)

Absolutely unstable behaviour is clearly depicted in figure 16(e), since the edges of the disturbance wavepacket are moving in opposite directions. The large-time asymptotic value of the spatial wavenumber for the disturbance in the homogenized flow was estimated using the simulation data to be $\alpha_0 \approx 0.34 - \mathrm{i}0.12$. The value of the leading-edge velocity U_L could be estimated by examining the gradient of the sharp leading edge of the disturbance wavepacket that is displayed in figure 16(e). This yielded $U_L Re \approx 100$. Using the relationships stated in (4.17), it was then possible to obtain the estimate $(1/\gamma Re)_r \approx 0.005$ (and also $U_T Re \approx -2$). From estimates for the real and imaginary parts of the radial derivative of the wavenumber α in (4.18), it was found that $\gamma_i/\gamma_r \approx 1.6$. Hence, we have $1/\gamma Re \approx 0.005 - \mathrm{i}0.008$. This confirms the necessity of including dispersion effects as well as diffusion effects in the modelling, through the use of complex values for the parameter γ that multiplies the second-order spatial derivative term in the Ginzburg–Landau equation.

Figures 16(b) and 16(d) display the variation of the temporal frequencies and growth rates predicted by the impulse solution of the Ginzburg–Landau equation that was constructed, for the homogenized flow, using the estimated values for ω_0, α_0 and γ. The spatial–temporal development of the disturbance wavepacket obtained for the same impulse solution is shown in figure 16(f). As in previous figures, the frequencies and growth rates are plotted for four equally spaced radial positions. Because of the presence of a reflective symmetry about the shifted impulse location $r = 0$ in (4.14) when $\mu_1 = 0$, the curves for the radial positions $r_e - 25$ and $r_e + 25$ coincide. This exact symmetry does not hold for the numerical simulation results. However, the differences are easily explained after it is realized that asymmetric behaviour can be obtained if a smeared impulse distribution is imposed, instead of point forcing, when the appropriate solution of the Ginzburg–Landau equation is determined. (Reference may be made to Thomas 2007 for further details.) By necessity, the impulse used in the numerical simulations had to be spread over a finite range of radial grid positions in order for it to be fully resolved, though this spread was kept as small as possible.

Having specified the parameters ω_0, α_0 and γ by utilizing simulation data for the radially homogenized flow, a value for μ_1 was found with the aid of data from the corresponding numerical simulation for the inhomogeneous flow. The estimation method made use of the asymptotic radial variation of the complex frequency, in the manner described at the end of the previous subsection. An alternative estimate for μ_1 was obtained using data from homogenized-flow simulations conducted at different Reynolds numbers, making use of (4.20). Both methods of estimation gave quite similar results and suggested the choice of the value $\mu_1 Re \approx 0.007 - \mathrm{i}0.019$.

The numerical simulation results for the temporal frequencies, growth rates and spatial–temporal development of the disturbance wavepacket that were obtained for the genuine radially dependent flow are plotted in figures 17(a), 17(c) and 17(e), respectively. The frequencies, growth rates and disturbance wavepacket development derived from the fitted impulse function (4.10) are shown for comparison in figure 17(b,d,f). It may be seen that the predicted behaviour for the frequencies

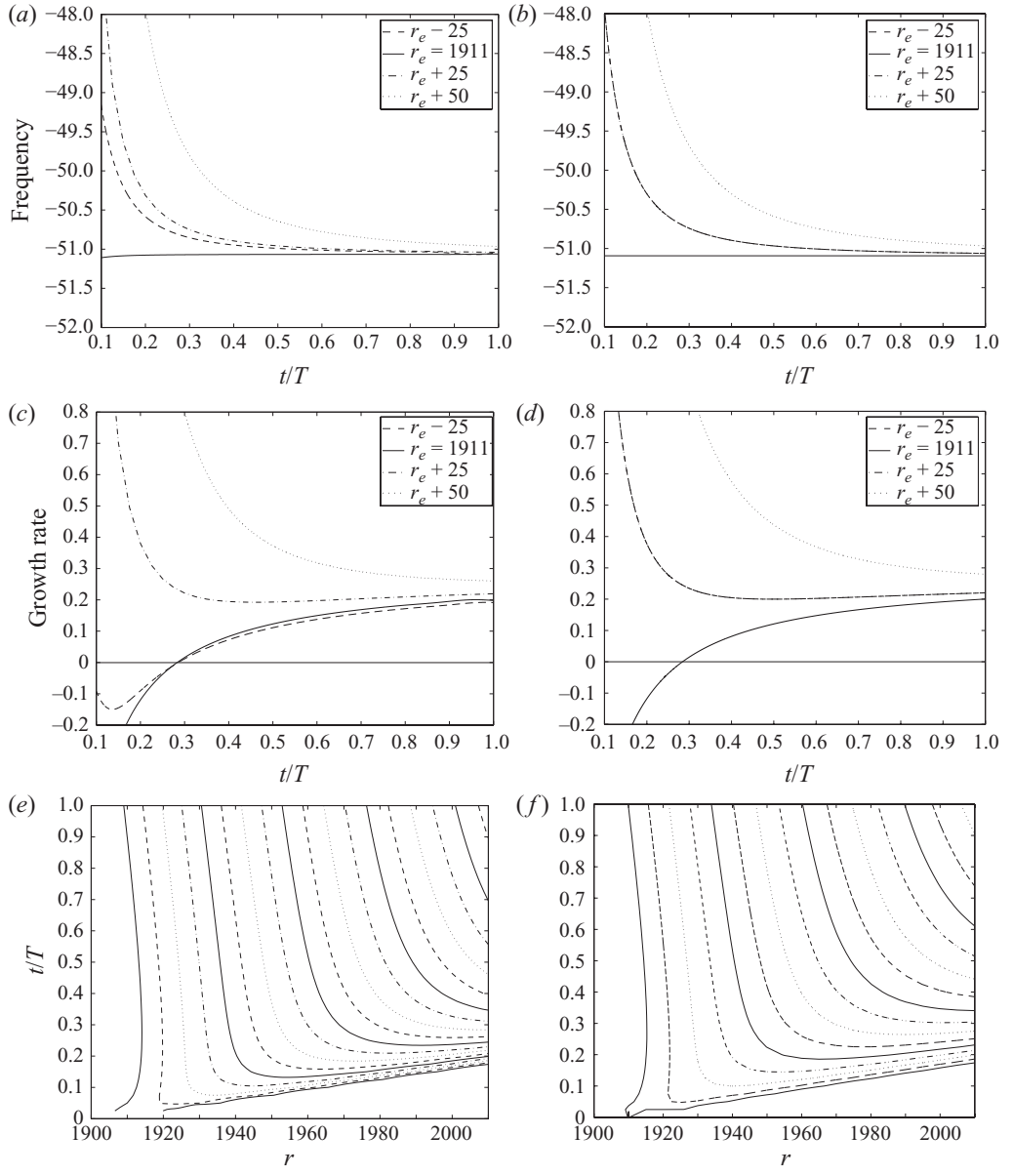

FIGURE 16. Local temporal frequencies $\omega_r Re$, temporal growth rates $\omega_i Re$ and disturbance wavepacket contours for the radially homogenized flow with suction $\boldsymbol{a} = 1$. $Re = 1911$ and $n = 194$. (*a*,*c*,*e*) Numerical simulation results. (*b*,*d*,*f*) The corresponding results obtained using the fitted impulse solution of the Ginzburg–Landau equation (4.10), with $\mu_1 = 0$. The frequencies and growth rates are plotted for four equally spaced radial positions. The wavepacket contours displayed for the simulation represent the azimuthal vorticity at the disk surface.

and growth rates is in good qualitative agreement with the results of the numerical simulations; for instance, they all eventually increase. The degree of quantitative agreement is also quite strong. It may be observed that the forms taken by the disturbance wavepacket contours are very similar to each other. Behaviour that is indicative of global instability is displayed in both cases. It may thus be surmised

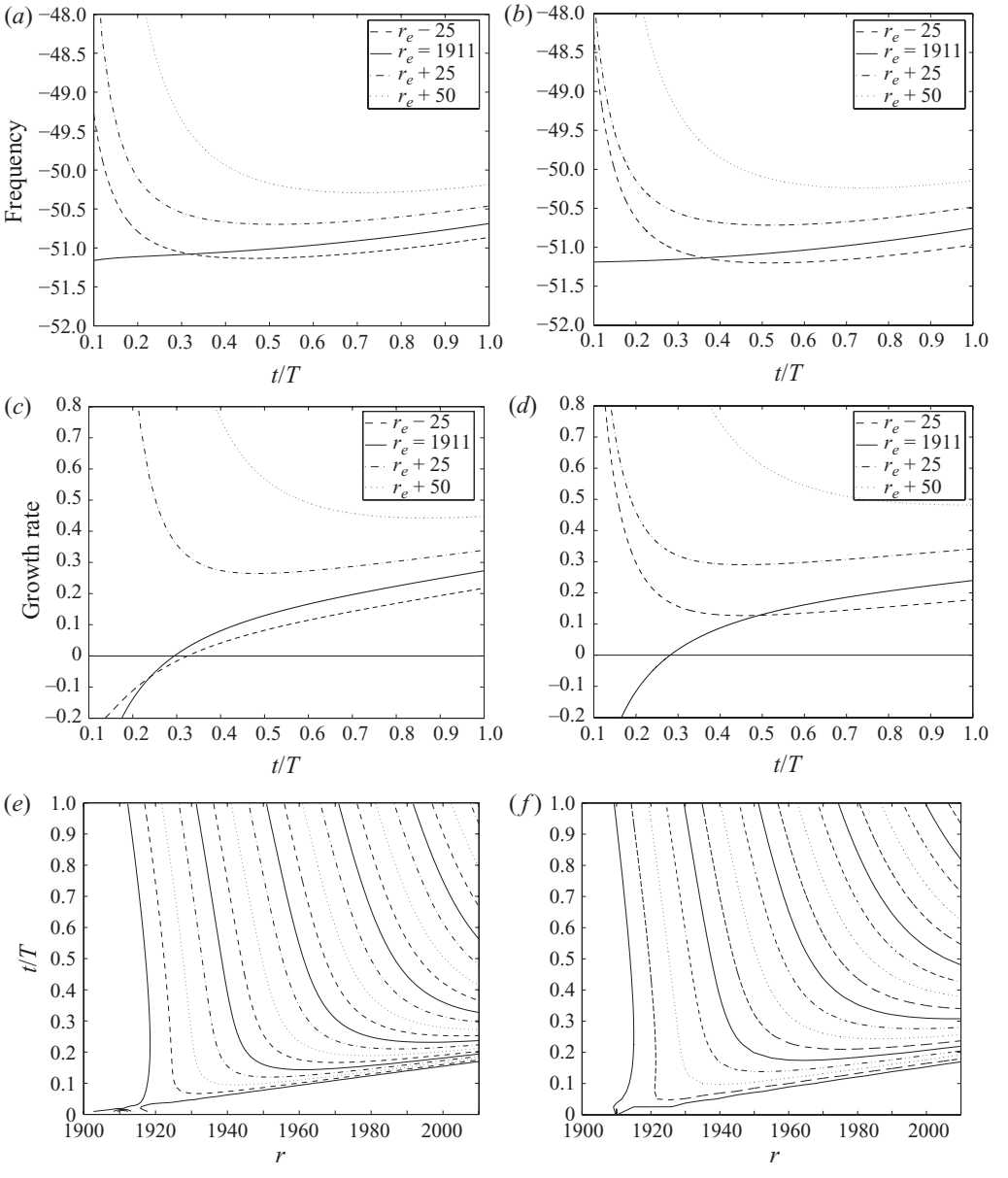

FIGURE 17. Local temporal frequencies $\omega_r Re$, temporal growth rates $\omega_i Re$ and disturbance wavepacket contours for the inhomogeneous flow with suction $\boldsymbol{a} = 1$. The impulse was excited at $r_e = 1911$ and $n = 194$, as in figure 16. (*a*,*c*,*e*) Numerical simulation results. (*b*,*d*,*f*) Results obtained using the fitted impulse solution of the Ginzburg–Landau equation (4.10), with μ_1 taken to be non-zero so as to model the radial inhomogeneity of the flow.

that the introduction of a single complex constant μ_1 has allowed the differences between the behaviour of the disturbances in the genuine flow and the artificial flow to be successfully modelled. The changes in behaviour are captured both qualitatively and quantitatively; the latter with a surprising degree of accuracy, given the relative simplicity of the Ginzburg–Landau equation modelling and the unoptimized nature of the fitting procedure that was adopted.

5. Perspectives for nonlinear studies

Note that all of the results presented here are for the case of linearized disturbances. Further numerical simulations for finite-amplitude disturbances would be useful in investigating the role of nonlinearity, for a range of possible laminar–turbulent transition routes that might be observed in rotating-disk experiments, with various different physical configurations and initial disturbance environments.

For instance, the previously mentioned theoretical study by Pier (2003) indicates that, for the case without mass transfer, a nonlinear global mode can be constructed, which will itself become subject to a strong form of secondary absolute instability. The secondary absolute instability may, in turn, be expected to trigger the transition to a turbulent flow. However, there is an implicit assumption in Pier's analysis that the effects of the radial inhomogeneity of the base flow are insufficient to interfere with the operation of the primary absolute instability that would serve to create the nonlinear global mode. Nonlinear numerical simulation studies could be helpful in establishing the conditions for the validity of this assumption. More generally, there is a need for additional work to be undertaken in order to determine the consequences of interchanging the approximations of linearity and flow homogenization in the preliminary stages of the development of any nonlinear theory. Pier's work can be construed as only considering the effects of the underlying inhomogeneity of the base flow after nonlinearity has been taken into account. Our linearized numerical simulations, on the other hand, include the effects of radial inhomogeneity before any account of nonlinearity is taken. The results obtained from these simulations indicate that, for the whole class of rotating flows with mass injection, as well as for the flow without mass transfer, absolutely unstable disturbances with a sufficiently small initial amplitude may never be able to grow large enough for nonlinearity to come into play in the manner that Pier presumes.

The importance of incorporating the effects of radial inhomogeneity into any nonlinear theory can also be inferred from the results of the physical experiments conducted by Othman & Corke (2006). For the case without mass transfer, they found no evidence for nonlinear global modes, or any subsequent secondary absolute instability, when the initial disturbance amplitudes were taken to be sufficiently small. In fact, as mentioned in the introduction, laminar flow was found to persist considerably beyond the critical Reynolds number for the onset of absolute instability. All of this is consistent with the hypothesis that nonlinear disturbance development may be forestalled in cases where there is a global linear stabilization associated with the base-flow inhomogeneity. Unfortunately, Othman & Corke (2006) were unable to fully categorize the nonlinear behaviour that ensued when they increased the amplitude of the disturbances that were introduced into the flow; no unequivocal evidence was obtained for the existence of an initial disturbance amplitude threshold, above which nonlinear global modes and secondary absolute instability could arise. In view of this, it is pertinent to mention a recent study for a related boundary-layer flow configuration. Viaud, Serre & Chomaz (2008) report results obtained from nonlinear numerical simulations that were conducted for flows confined between two rotating disks. As in our linearized simulations, the base flows were inhomogeneous along the radial direction. It was discovered that nonlinear global modes could only be manifested in the simulations when the initial disturbance amplitude, used in seeding the primary absolute instability, was taken to be sufficiently large.

We end this section with a few remarks that have a particular bearing on the disturbance development when there is a global linear destabilization due to the base-flow inhomogeneity, as was found for the rotating disk boundary layers with

a strong enough level of suction. Theoretical analysis for spatially inhomogeneous base flows often uses, as one of its starting points, the well-known result that the existence of a region of absolute instability is a necessary, but not in general sufficient, condition for there to be a linearly unstable global mode (see, for example, the reviews by Huerre 2002 and Chomaz 2005, which list many further relevant references). This necessary condition does not, at least at first sight, seem to fit very well with our observations of a form of global instability that involves the propagation of temporally growing disturbances into radially inboard regions where the flow is known to be absolutely stable. The apparent conflict can be resolved by simply noting that global modes are usually taken, by definition, to have a well-defined temporal frequency, which is selected by the character of the absolute instability. No such frequency selection occurred for the impulsively excited disturbances that we simulated in the inhomogeneous rotating-disk boundary-layer flows. The oscillation frequencies associated with the disturbances were found to vary over time, as well as being dependent upon the radial location, in all of the flows that we considered. This included the suction-flow cases where there was continual temporal growth. The incorporation of such a previously unsuspected kind of temporal instability presents an interesting challenge for any future theoretical approach to nonlinear disturbance evolution. It is even conceivable that the novel nature of the unstable linearized disturbance development may discount the possibility of any analytical approach to nonlinearity that, in the interests of tractability, tries to postpone the inclusion of the effects of the inhomogeneity of the base flow. The destabilizing effects of the radial inhomogeneity may need to be accounted for from the outset of the analysis, irrespective of the initial disturbance amplitude.

6. Conclusions

A study has been carried out concerning the effects that disk surface mass transfer has on the global behaviour associated with the absolute instability of the rotating-disk boundary layer. This extends the previous investigations made by Davies & Carpenter (2003) and Davies *et al.* (2007), who considered the rotating-disk flow without any mass transfer. For flows with mass injection, the results obtained from numerical simulations were qualitatively similar to those that had been obtained previously. The radial inhomogeneity of the genuine flow was again found to have a stabilizing effect on the global disturbance development. No globally unstable forms of behaviour were detected for the absolute instability.

However, it was discovered that rotating-disk flows with mass suction could be destabilized by the effects of radial inhomogeneity. The simulations showed that for flows with a strong enough level of suction, disturbances excited within the absolutely unstable region could propagate radially inwards with a trailing edge which moved away from the impulse location at a radial velocity that became increasingly negative. These disturbances also exhibited increasingly rapid temporal growth. Such behaviour is indicative of the presence of global instability. However, there was no selection of any global temporal frequency, as might have been anticipated more usually for a globally unstable flow.

The results of this study might appear to be rather counterintuitive. An analysis of the radially homogenized version of the rotating-disk boundary layer shows that mass suction has a strong stabilizing effect on the absolute instability, postponing its onset to higher Reynolds numbers. However, for the genuine radially inhomogeneous flow, the advantageous stability effects of mass suction appear to come with the risk

of the introduction of global instability. In an oppositely directed, yet similar fashion, it was found that the destabilizing effects of mass injection that are predicted for the homogenized flow can be overcome to yield a global stabilization in the genuine flow.

The above results may help to explain why previous experimental investigators (Gregory & Walker 1960) were unable to use suction to extend the laminar flow region for the rotating-disk boundary layer as far as might have been expected. Since the numerical simulations show that suction promotes a novel form of globally unstable behaviour, it is possible that this may lead to a lowering of the radius associated with the onset of transition to turbulence, reducing it below the critical value for absolute instability that is predicted using a linear stability analysis based upon the homogenized-flow approximation (Lingwood 1997). However, roughness imperfections introduced into the disk surface, due to the need to apply an approximately uniform level of suction through it, are also likely to have reduced the radial extent of the laminar flow in the physical experiment. Thus, it is difficult to determine, retrospectively, whether or not the globally unstable behaviour that we have simulated could have played any significant role. There is a need for further physical experiments to be conducted, making use of improvements in experimental technology in order to more carefully control the effects of disk surface roughness.

We have shown that the global behaviour of absolutely unstable disturbances in the rotating-disk boundary layer can be modelled and explained, heuristically at least, using impulse solutions of the linearized Ginzburg–Landau equation. The terms included in the model can be chosen so that they measure the influences of temporal growth and oscillation, flow convection, diffusion and dispersion. The global characteristics of a disturbance can then be determined through an examination of the balance that persists between the effects of radial variations in temporal growth rates, radial variations in the temporal frequencies and the effects of diffusion and dispersion. The form of this balance suggests how it can be possible for an absolutely unstable rotating-disk boundary layer flow to either remain globally stable or to become globally unstable in a manner that leads disturbances to grow at an increasingly rapid rate. It is worth noting that the stabilizing effect of local variations in frequency on otherwise neutrally stable disturbances, known as 'phase-mixing', has been familiar to many in the astrophysical fluids research community for quite some time (see, for example, Soward 1977, 1992 and Harris, Bassom & Soward 2000).

This work was supported by the Engineering and Physical Sciences Research Council. The authors would like to thank Professor A. Bassom of the University of Western Australia for his many helpful suggestions for improving this paper.

REFERENCES

Batchelor, G. K. 1951 Note on a class of solutions of the Navier–Stokes equations representing steady rotationally-symmetric flow. *Q. J. Mech. Appl. Math.* **4**, 29–41.

Briggs, R. J. 1964 *Electron–Stream Interactions in Plasmas*. MIT Press.

Chomaz, J. M. 2005 Global instabilities in spatially developing flows: non-normality and nonlinearity. *Annu. Rev. Fluid Mech.* **37**, 357–392.

Davies, C. & Carpenter, P. W. 2001 A novel velocity–vorticity formulation of the Navier–Stokes equations with applications to boundary layer disturbance evolution. *J. Comp. Phys.* **172**, 119–165.

Davies, C. & Carpenter, P. W. 2003 Global behaviour corresponding to the absolute instability of the rotating-disc boundary layer. *J. Fluid Mech.* **486**, 287–329.

Davies, C., Thomas, C. & Carpenter, P. W. 2007 Global stability of the rotating disc boundary layer. *J. Engng Math.* **57** (3), 219–236.

Faller, A. & Kaylor, R. 1966 A numerical study of the instability of the laminar Ekman boundary layer. *J. Atmos. Sci.* **23**, 466–480.

Gajjar, J. S. B. 1996 On the nonlinear evolution of a stationary cross-flow vortex in a fully three-dimensional boundary layer flow. In *Nonlinear Instability and Transition in Three-Dimensional Boundary Layers, IUTAM Symposium, Manchester, UK, 1995* (ed. P. W. Duck & P. Hall), pp. 317–327. Kluwer.

Gajjar, J. S. B., Arebi, M. A. & Sibanda, P. 1996 Nonlinear development of cross-flow instabilities in compressible and incompressible boundary layer flows. *AIAA Paper* 96-2159.

Gray, W. E. 1952 The nature of the boundary layer at the nose of a swept back wing. Min. Aviation, London (unpublished).

Gregory, N., Stuart, J. T. & Walker, W. S. 1955 On the stability of three-dimensional boundary layers with application to the flow due to a rotating disk. *Philos. Trans. R. Soc. Lond.* A **248**, 155–199.

Gregory, N. & Walker, W. S. 1960 Experiments on the effect of suction on the flow due to a rotating disk. *J. Fluid Mech.* **9**, 225–234.

Hall, P., Malik, M. R. & Poll, D. I. A. 1984 On the stability of an infinite attachment line boundary layer. *Proc. R. Soc. Lond.,* A **395**, 229–245.

Harris, D., Bassom, A. P. & Soward, A. M. 2000 An inhomogeneous Landau equation with application to spherical Couette flow in the narrow gap limit. *Physica* D **137**, 260–276.

Huerre, P. 2002 Open shear flow instabilities. In *Perspectives in Fluid Dynamics* (ed. G. K. Batchelor, H. K. Moffatt & M. G. Worster), pp. 159–229. Cambridge University Press.

Hunt, R. E. & Crighton, D. G. 1991 Instability of flows in spatially developing media. *Proc. R. Soc. Lond.* A **435**, 109–128.

von Kármán, T. 1921 Über laminare und turbulente Reibung. *Z. Angew. Math. Mech.* **1**, 233–252.

Lingwood, R. J. 1995 Absolute instability of the boundary layer on a rotating disk. *J. Fluid Mech.* **299**, 17–33.

Lingwood, R. J. 1996 An experimental study of absolute instability of the rotating-disk boundary-layer flow. *J. Fluid Mech.* **314**, 373–405.

Lingwood, R. J. 1997 On the effects of suction and injection on the absolute instability of the rotating-disk boundary layers. *Phys. Fluids* **9**, 1317–1328.

Mack, L. M. 1985 The wave pattern produced by point source on a rotating disk. *AIAA Paper* 85-0490.

Malik, M. R. 1986 The neutral curve for stationary disturbances in rotating-disk flow. *J. Fluid Mech.* **164**, 275–287.

Othman, H. & Corke, T. 2006 Experimental investigation of absolute instability of a rotating-disk boundary layer. *J. Fluid Mech.* **565**, 63–94.

Pier, P. 2003 Finite amplitude crossflow vortices, secondary instability and transition in the rotating disk boundary layer. *J. Fluid Mech.* **487**, 315–343.

Soward, A. M. 1977 On the finite amplitude thermal instability of a rapidly rotating sphere. *Geophys. Astrophys. Fluid Dyn.* **9**, 19–74.

Soward, A. M. 1992 Thin disc kinematics $\alpha\omega$-dynamo models. Part 2. Short length scale modes. *Geophys. Astrophys. Fluid Dyn.* **64**, 201–225.

Sparrow, E. M. & Gregg, J. L. 1960 Mass transfer, flow, and heat transfer about a rotating disk. *J. Heat Transfer* **82**, 294–302.

Stuart, J. T. 1954 On the effects of uniform suction on the steady flow due to a rotating disk. *Q. J. Mech. Appl. Math.* **7**, 446–457.

Thomas, C. 2007 Numerical simulations of disturbance development in rotating boundary layers. PhD thesis, Cardiff University.

Viaud, B., Serre, E. & Chomaz, J. M. 2008 The elephant mode between two rotating disks. *J. Fluid Mech.* **598**, 451–464.